JGR Oceans

RESEARCH ARTICLE
10.1029/2024JC021103

Sand Dunes as a Nature-Based Solution to Mitigate Salt Intrusion in Stratified Estuaries

Sem J. Geerts[1,2], Wessel M. van der Sande[1], Suzanne J. M. H. Hulscher[1], Bernard J. Geurts[2], and Pieter C. Roos[1]

[1]Water Engineering and Management, Faculty of Engineering Technology, University of Twente, Enschede, The Netherlands, [2]Mathematics of Multiscale Modelling and Simulation (3MS), Faculty of Electrical Engineering, Mathematics and Computer Science, University of Twente, Enschede, The Netherlands

Key Points:

- Estuarine sand dunes decrease salt intrusion by an increase in turbulence causing more mixing
- The reduction in salt intrusion length is strongest for higher and shorter dunes
- The mitigating effect of sand dunes decreases when the estuary is less stratified

Correspondence to:
S. J. Geerts,
s.j.geerts@utwente.nl

Citation:
Geerts, S. J., van der Sande, W. M., Hulscher, S. J. M. H., Geurts, B. J., & Roos, P. C. (2025). Sand dunes as a nature-based solution to mitigate salt intrusion in stratified estuaries. *Journal of Geophysical Research: Oceans*, *130*, e2024JC021103. https://doi.org/10.1029/2024JC021103

Received 20 MAR 2024
Accepted 2 JAN 2025

Author Contributions:
Conceptualization: Wessel M. van der Sande, Suzanne J. M. H. Hulscher, Pieter C. Roos
Data curation: Sem J. Geerts
Formal analysis: Sem J. Geerts
Funding acquisition: Suzanne J. M. H. Hulscher, Pieter C. Roos
Methodology: Sem J. Geerts
Project administration: Suzanne J. M. H. Hulscher, Pieter C. Roos
Software: Sem J. Geerts
Supervision: Wessel M. van der Sande, Suzanne J. M. H. Hulscher, Bernard J. Geurts, Pieter C. Roos
Validation: Sem J. Geerts
Visualization: Sem J. Geerts
Writing – original draft: Sem J. Geerts
Writing – review & editing: Sem J. Geerts, Wessel M. van der Sande, Suzanne J. M. H. Hulscher, Bernard J. Geurts, Pieter C. Roos

Abstract Salt intrusion in estuaries can pose a threat to drinking water extraction, irrigation, industries, and ecology. Key factors influencing the salt intrusion length include freshwater river flushing and vertical salt mixing. This study investigates the potential of estuarine sand dunes, that is, large-scale rhythmic patterns, to serve as a nature-based solution to mitigate salt intrusion. To this end, we adopt a two-dimensional vertical (2DV) modeling approach, which numerically solves the flow and salt transport in an idealized single-channel estuary. By varying the tidal amplitude and river discharge, three types of estuaries are modeled; a salt wedge, a strongly stratified and a strain-induced periodic stratification estuary. Two types of dune configurations are considered: 'depth-neutral' dunes (preserving mean water depth) and 'deepening' dunes (crest level equal to original bed level, rest of dune profile entirely below). Model results demonstrate that the presence of dunes can effectively reduce the salt intrusion length by several kilometers, compared to the scenario without dunes. Systematically varying dune geometry demonstrates that steeper (higher and shorter) dunes yield a stronger reduction in the salt intrusion length. Deepening dunes have the potential to generate sufficient mixing to overcome the adverse effects of channel deepening and, as such, can mitigate salt intrusion while maintaining navigability. As a naturally existing bedform, estuarine sand dunes present a promising nature-based solution against salt intrusion without compromising accessibility to seaports.

Plain Language Summary Estuaries are water bodies near the coast where saline seawater mixes with fresh runoff water. As saline water is denser, it intrudes beneath the outflowing river water and moves inland, a phenomenon known as salt intrusion. This puts stress on industries and the extraction of drinking water. Estuarine sand dunes are wave-shaped sandy bedforms that decrease the water depth for ships when they grow in height. Therefore, these sand dunes are often dredged away for navigability. The channel is deepened during dredging which increases salt intrusion. In this study, we simulate and aim to understand the influence of estuarine sand dunes on salt intrusion. We find that with larger and shorter dunes, salt intrusion decreases as more salt is mixed in the water column and flushed out by the river discharge. Furthermore, if dunes are artificially created smartly, that is, by dredging beneath the required bed level for shipping, we show that it is possible to retain the navigability of the waterways while simultaneously decreasing salt intrusion. Hence, these naturally occurring bedforms inspire a nature-based solution to mitigate salt intrusion.

1. Introduction

Estuaries are semi-enclosed embayments of the coast in which tidal waves propagate through a system of channels which discharges freshwater runoff from inland. The dynamic interaction and mixing of saline water and freshwater runoff leads to salt intrusion (MacCready & Geyer, 2010; Valle-Levinson, 2010), where denser seawater intrudes inland beneath outflowing riverine freshwater. This salt intrusion forms the central focus of our investigation, quantified by the salt intrusion length. Significant salt intrusion can cause a shortage of fresh water, affecting industries, agriculture, and the accessibility of drinking water (Mekonnen & Hoekstra, 2016). The demand for freshwater for anthropogenic activities is increasing (Wada et al., 2011) and salt intrusion is enhanced by the multifaceted impacts of climate change, including rising sea levels, storm set-up, variability in river discharge and increased drought occurrences (Veldkamp et al., 2015). Estuaries are important environments in the coastal zone (Lotze, 2010). They connect the sea to inland waterways and, thus, form an ideal location for large seaports. The Rotterdam Waterway (RWW) in the Netherlands is an example of a highly industrialized estuary, accommodating the largest port in Europe (Kammoun & Abdennadher, 2022). To ensure navigability and to

counteract sedimentation, the main channel is frequently dredged, deepening the channel and flattening the bed to ensure a minimum water depth (Cox et al., 2021). This engineered estuary forms the inspiration of this idealized study, in which we focus on the influence of estuarine sand dunes on the salt intrusion length.

Salt intrusion results from the competition between river flow transporting salt downstream and several processes transporting salt upstream (Geyer & MacCready, 2014). These upstream-directed processes consist of tidal pumping, lateral processes and estuarine circulation, the latter mostly comprised the ESCO circulation and gravitational circulation (Dijkstra et al., 2017). The outward salt transport by river flow flushes salt out of the system. Hence, an increase in channel depth greatly increases salt intrusion by a reduction of the mean river flow velocity (Ralston & Geyer, 2019). In the presence of significant stratification, the dominant mechanism responsible for removing salt during each tidal cycle is the vertical salt flux, rather than the seaward advection of high-salinity fluid (MacDonald & Horner-Devine, 2008). Vertical mixing diminishes stratification, allowing salt to be transported up in the water column and flushed out. Consequently, factors contributing to an increased vertical mixing, such as bottom roughness and reduced water depth, generally reduce the salt intrusion length (Hendrickx et al., 2023). Correspondingly, dredging activities that increase the water depth and reduce vertical variation of the bed possibly increase salt intrusion by reducing river flushing and vertical mixing.

Nature-based solutions leverage natural systems and dynamics to address society's needs while creating room for nature development (de Vriend et al., 2015). These solutions often have lower costs than traditional engineering solutions on a life-cycle basis (Borsje et al., 2011). In recent years, research on salt intrusion has been directed toward understanding the system and its natural processes, which forms the first step in the development of nature-based solutions (e.g., Hendrickx et al., 2023).

Estuaries exhibit unique physical processes that influence the development of bedforms. Of particular interest are estuarine sand dunes, analogous to river dunes in inland waterways and tidal sand waves in marine environments. The geometry and dimensions of these three types of bedforms are largely similar, but the morphological processes differ as estuaries are subject to both river forcing and tides. Besides, salinity gradients play a crucial role in influencing the growth, typical wavelengths, and migration rates of sand dunes (van der Sande et al., 2021; van der Sande et al., 2023). They are observed in, for example, the Gironde estuary (France) (Berné et al., 1993), Elbe estuary (Germany) (Zorndt et al., 2011), Fraser River estuary (Canada) (Bradley et al., 2013) and Weser River estuary (Germany) (Lefebvre et al., 2022). Typical dune heights are around 10% of the water depth, and dune lengths range from 30 to 180 m in water depths ranging from 12 to 20 m (Berné et al., 1993; Bradley et al., 2013; Lefebvre et al., 2022; Zorndt et al., 2011). The deeper part of the RWW does show some permanent ridges with similar characteristics as sand dunes, but an extensive dune field has not been found (Pietrzak et al., 1991). Field studies indicate that estuarine sand dunes potentially increase the net vertical salt flux, by an increase in turbulence (Best et al., 2001; Bradley et al., 2013) and breaking of resonant internal waves (Kostaschuk et al., 2010; Pietrzak et al., 1990). Sand wave models show the presence of tide-averaged circulation cells (Németh et al., 2002), likely also present over estuarine sand dunes (Hulscher & Dohmen-Janssen, 2005). Due to their natural occurrence and their capacity to generate additional vertical mixing, these estuarine sand dunes potentially present a nature-based solution to mitigate salt intrusion.

Idealized salinity models have been used to explore the dominant processes responsible for salt dynamics in estuaries (e.g., Biemond et al., 2022; Dijkstra et al., 2022; Jongbloed et al., 2022). These studies highlight the sensitivity of the salt transport processes to the channel depth and bed friction and show the importance of gravitational circulation for the landward transport of salt in the RWW. However, turbulence is strongly simplified in these models and the models are currently unsuitable for the explicit implementation of sand dunes. Complex numerical models provide a more detailed assessment of salt intrusion at the scale of entire estuaries and can include the interaction of turbulence and stratification (e.g., Hendrickx et al., 2023). Veerapaga et al. (2019) used a 3D numerical model to study the effect of sinusoidal bedforms on the salt intrusion length in a stratified estuary of 4 m depth. Relatively low-angled dunes with long wavelengths ($\geq$350 m) are implemented. They find that salt intrusion length decreases with shorter and larger dunes, which is attributed to enhanced vertical mixing due to trapped salt water in the troughs that is entrained during ebb.

In this research, we aim to understand how estuarine sand dunes affect salt dynamics in terms of the salinity structure and salt transport, and how this depends on the dune geometry and the type of estuary. From a practical perspective, we thus investigate the potential of dunes to serve as a nature-based solution to mitigate salt intrusion. This is examined through an idealized process-based numerical model, which contains essential processes such as

tidal flow, river flow and turbulence. We assume that the main transport processes occur in the longitudinal and vertical direction (Biemond et al., 2023; Dijkstra et al., 2022); sand dune geometry is schematized in the same two dimensions (Lokin et al., 2022; Zorndt et al., 2011). Hence, we formulate a numerical model in which a single-channel estuary is modeled in a longitudinal vertical plane (or 2DV) and lateral effects are neglected. The flow is modeled with the hydrostatic shallow-water equations. The model is designed for estuarine systems that can be approximated as a single-channel estuary with uniform nonconvergent geometry. In this study, the model geometry is inspired by the RWW, an estuary that ranges from strongly stratified (SS) in summer to a salt wedge (SW) in winter (de Nijs et al., 2011). With this model, we systematically vary dune characteristics (wavelength, height, and asymmetry) to determine the change in salinity transport and the salt intrusion length. We consider two types of dune configuration relative to the initial bed level; 'depth-neutral' dunes (preserving mean water depth) and 'deepening' dunes (crest level equal to original bed level, with the rest of dune profile entirely below). Lastly, we consider three types of stratified estuaries; strain-induced periodic stratification (SIPS), SS, and a SW estuary by varying the boundary conditions (MacCready & Geyer, 2010).

The remainder of this paper is organized as follows. In Section 2, we present the model description, implementation and methodology of analysis. Section 3 contains the results, distinguishing between the influence of the following aspects: boundary conditions on salinity structure, presenting three different types of estuaries (Section 3.1); dune geometry on the salt intrusion length (while preserving mean depth) (Section 3.2); deepening dune height on salt intrusion (while maintaining navigability) (Section 3.3). Section 3.4 describes how the salt intrusion length and changes in dune geometry are related to the hydrodynamic and turbulent processes. Section 4 contains the discussion and conclusions are drawn in Section 5.

2. Methods: Model Formulation and Analysis

2.1. Model Geometry

The estuary's geometry is a single channel of uniform width, with length L (Figure 1a). Lateral effects are neglected and a longitudinal vertical plane (2DV) model is used. The horizontal along-channel coordinate x is defined from the estuary mouth at $x = 0$ to the riverine boundary at $x = L$ well inland. The vertical coordinate z points upward, with the reference level of the free surface elevation at $z = 0$ and the reference bed level at $z = -h$. Throughout our study, the estuary length and reference depth are kept constant to $L = 50$ km and $h = 15$ m.

The model is morphostatic, no average bed slope is present and the topography is defined by $z = z_b$. The free surface elevation is denoted with η, and the instantaneous water depth (varying over time t and x) reads

$$H(x,t) = \eta(x,t) - z_b(x). \tag{1}$$

The flow velocity is denoted by horizontal component $u(x,z,t)$ and vertical component $w(x,z,t)$. Salinity is denoted by $s(x,z,t)$ in ppt (parts per thousand), affecting density by the equation of state $\rho(x,z,t) = \rho(s(x,z,t))$, for which the UNESCO (1981) formulation is used.

In the model, sand dune shapes are idealized and Figure 1b visualizes a single sand dune and the relevant dimensions to describe its shape. The dune height H_d is defined as the vertical distance from trough to crest and dune length λ_d is the horizontal distance between two adjacent troughs. The lee and stoss sides of the dune are defined relative to the river flow direction and their lengths are denoted by λ_l and λ_s , respectively. Note that in this model set-up, the stoss side has a negative slope ($dz_b/dx < 0$).

We examine the influence of estuarine sand dunes using two types of dune configurations relative to the reference level $z = -h$, as visualized by Figure 1c. We distinguish between **depth-neutral dunes** and **deepening dunes**, which are differentiated and defined by the type of depth that is maintained when the dune height increases. Depth-neutral dunes *maintain mean depth* and are specified by the deepening parameter $D = 0$. Contrarily, deepening dunes keep the crest level at a constant reference level for different dune dimensions, and thus *maintain navigable depth* (while increasing the mean depth), using $D = 1$.

The topography z_b is defined by a dune field with uniformly shaped dunes. All geometry configurations are captured by a single bed level function

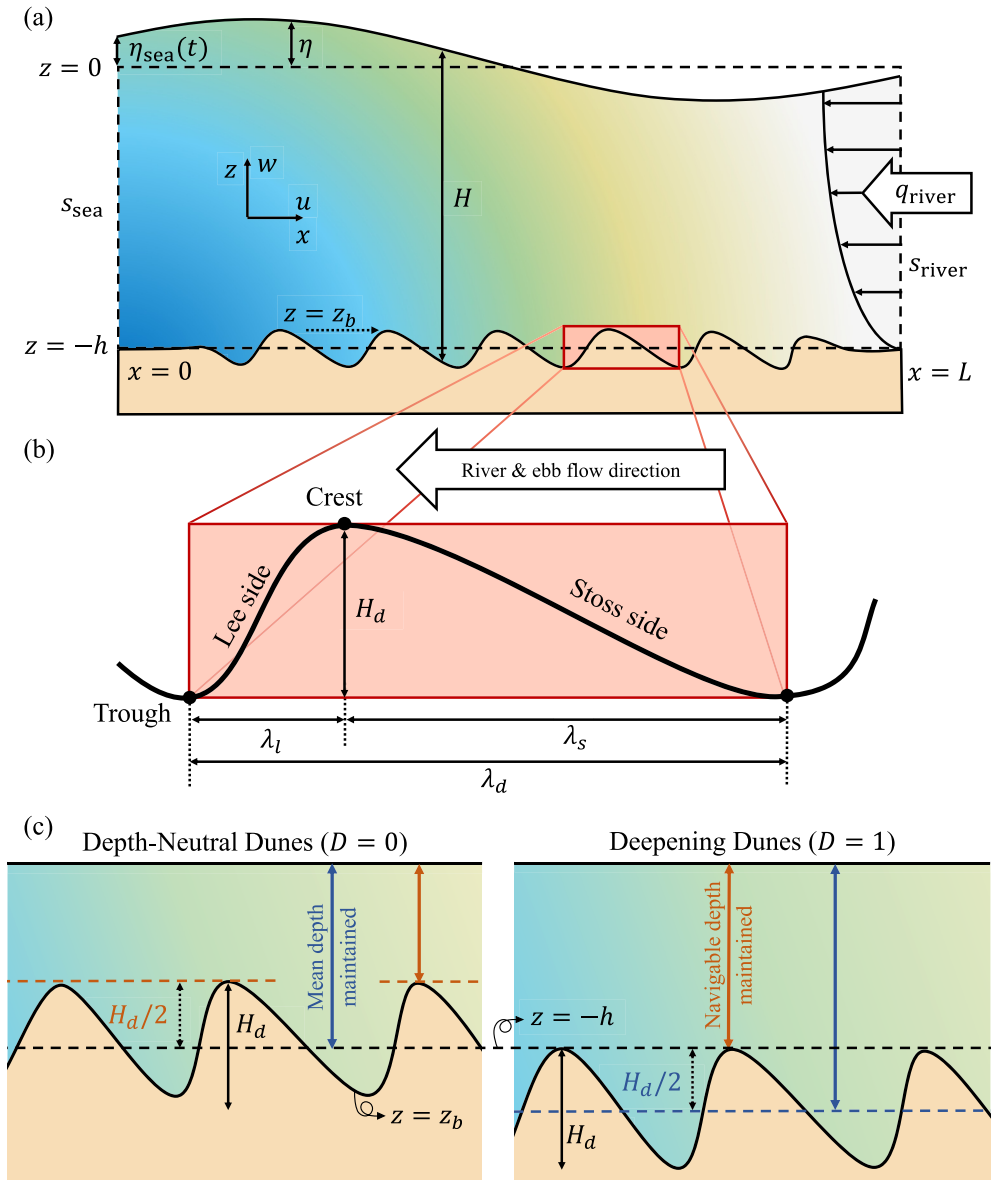

Figure 1. Overview of the model setup. Note that the vertical scale is exaggerated. (a) Schematization of the model geometry of the estuary, with seaward tidal elevation η_{sea} at $x = 0$ and inflowing river discharge q_{river} at the riverine boundary $x = L$. Background colors visualize salinity concentration and gradients from saline (blue) to fresh (white). (b) Schematization of estuarine sand dunes with dune height H_d and dune length λ_d, equal to the sum of the lee side and stoss side lengths λ_l and λ_s. The lee and stoss sides are defined relative to the river flow direction. (c) Visualization of the two dune configurations relative to reference level $z = -h$ for equal dune height H_d. Left: depth-neutral dunes that maintain mean depth ($D = 0$). Right: deepening dunes that maintain navigable depth ($D = 1$).

$$z_b(x) = -h + \frac{1}{2} H_d b(x)(\Lambda_d(x) - D), \tag{2}$$

where $b(x)$ is a nondimensional envelope function between 0 and 1 that ensures that changes relative to the reference level $z = -h$ are smoothly introduced at the tails of the dune field (Appendix A). The idealized dune profile Λ_d is described by the nondimensional shape formulation.

$$\Lambda_d(x) = \begin{cases} \sin(k_d x), & \text{if } \mathcal{A}_d = 0, \\ \frac{2}{\pi \mathcal{A}_d} \arctan\left(\frac{\sin\left(\frac{\pi}{2}\mathcal{A}_d\right) \sin(k_d x)}{1 - \sin\left(\frac{\pi}{2}\mathcal{A}_d\right) \cos(k_d x)} \right), & \text{if } \mathcal{A}_d \neq 0, \end{cases} \tag{3}$$

in which $k_d = 2\pi/\lambda_d$ denotes the dune wave number and

$$\mathcal{A}_d = \frac{\lambda_s - \lambda_l}{\lambda_d} \tag{4}$$

the dune asymmetry parameter (as in Knaapen, 2005), ranging from −1 to 1. Equation 3 yields a spatially periodic function with mean zero over wavelength λ_d, meaning that the total amount of sediment is conserved for different dune heights when depth-neutral dunes ($D = 0$) are considered. This idealized profile covers the entire dune geometry space and ensures that the maximum dune slope is reached halfway between trough and crest. Neither dune configuration changes the bed level at the open boundaries, where $b(x) = 0$ is fixed (Appendix A).

2.2. Model Equations and Boundary Conditions

The flow is modeled by the hydrostatic incompressible shallow-water equations (e.g., Klingbeil et al., 2022), given by

$$\frac{\partial u}{\partial x} + \frac{\partial w}{\partial z} = 0, \tag{5}$$

$$\frac{\partial u}{\partial t} + u\frac{\partial u}{\partial x} + w\frac{\partial u}{\partial z} = \frac{\partial}{\partial x}\left(A_h \frac{\partial u}{\partial x}\right) + \frac{\partial}{\partial z}\left(A_v \frac{\partial u}{\partial z}\right) - g\frac{\partial \eta}{\partial x} - g\int_z^\eta \frac{\partial \rho(x,\tilde{z},t)}{\partial x}\, d\tilde{z}, \tag{6}$$

where g represents the gravitational acceleration. The horizontal and vertical eddy viscosity are denoted by A_h and A_v, respectively. The transport of salt is modeled by the transport equation in conservative form according to

$$\frac{\partial s}{\partial t} + \frac{\partial}{\partial x}(su) + \frac{\partial}{\partial z}(sw) = \frac{\partial}{\partial x}\left(K_h \frac{\partial s}{\partial x}\right) + \frac{\partial}{\partial z}\left(K_v \frac{\partial s}{\partial z}\right), \tag{7}$$

where the horizontal and vertical eddy diffusivity are denoted by K_h and K_v, respectively. The turbulent eddy viscosity is determined by the k-ϵ turbulence model (presented in Appendix B1). In turn, the total eddy viscosities A_h and A_v and the eddy diffusivities K_h and K_v include these turbulent eddy effects, molecular effects and constant background values (see Appendix B2).

Salinity and flow are coupled in several ways. Horizontal baroclinic pressure gradients add a force to the momentum equation and accelerate the flow (last term in Equation 6). Indirectly, vertical salinity gradients (stratification) suppress the generation of turbulent kinetic energy (TKE) in the k-ϵ model (Appendix B1), decreasing the turbulent dispersion of salt (Geyer, 1993).

The seaward tidal elevation is assumed to be monochromatic, that is,

$$\eta(x,t) = \eta_{sea}(t) = A_{sea}\cos(\omega t), \quad \text{at } x = 0, \tag{8}$$

with tidal elevation amplitude A_{sea} and ω the angular frequency of the M2-tide. The horizontal velocity at the seaward boundary is solved by the momentum Equation 6 with zero momentum flux ($u\frac{\partial u}{\partial x} + w\frac{\partial u}{\partial z} = 0$). Inflowing water has salinity $s_{sea} = 35$ ppt.

At the inland riverine boundary $x = L$, a constant width-averaged river discharge q_{river} (in m^2/s) with constant salinity $s_{river} = 0$ ppt is imposed. We assume that the horizontal flow velocity at that boundary follows a logarithmic profile by

Table 1
Model Geometry, Constants, and Boundary Conditions for Each Estuary Type

Symbol	Description	Value	Units
L	Estuary length	50	km
h	Mean estuary depth	15	m
s_{sea}	Seaward salinity	35	ppt
s_{river}	Riverine salinity	0	ppt
ω	Angular frequency of M2-tide	$1.405 \cdot 10^{-4}$	rad s^{-1}
g	Gravitational acceleration	9.81	m s^{-2}

		SW[a]	SS[b]	SIPS[c]	
A_{sea}	Seaward tidal elevation amplitude	1.0	1.0	**2.5**	m
q_{river}	Width-averaged river discharge	**6.0**	1.5	1.5	m^2 s^{-1}

[a]Salt Wedge. [b]Strongly Stratified. [c]Strain-Induced Periodic Stratification.

$$u(x,z,t) = \frac{-q_{river}}{(H+z_0)\ln\left(\frac{H+z_0}{z_0}\right) - H} \ln\left(\frac{z+h+z_0}{z_0}\right), \qquad \text{at } x = L, \quad (9)$$

with roughness height $z_0 = 0.001$ m, corresponding to a Nikuradse roughness length of $k_s = 0.03$ m. Equation 9 imposes that the horizontal velocity is solely determined by the river discharge, which implies that the horizontal tidal flow velocity equals zero at the riverine boundary. As such, the estuary length L constitutes a length scale over which the tidal flow must have decayed. At both open boundaries, the vertical flow velocity over the water column is proportional to the change of the free surface and scales linearly over depth by

$$w(x,z,t) = \frac{z - z_b}{H} \frac{\partial \eta}{\partial t}, \qquad \text{at } x = 0, \text{ and } x = L. \quad (10)$$

At the free surface $z = \eta$, wind effects are neglected and zero shear (free slip) on the horizontal velocity is imposed. At the bed $z = z_b$, we impose a no-slip condition and the horizontal velocity is set to zero. The horizontal velocity near the bed is determined by a logarithmic law-of-the-wall function. No-normal-flux boundary conditions for flow and salinity are imposed at the bed and free surface (Klingbeil et al., 2022).

2.3. Overview of Parameter Settings

Table 1 provides the model settings used in this study. The estuary length and depth are based on the RWW. We consider three different types of stratification in the estuary by varying the seaward and riverine boundary conditions. Inspired by summertime flow conditions of the RWW, our reference case has an M2 tidal elevation amplitude of 1.0 m and riverine discharge $q_{river} = 1.5$ m^2/s, which leads to an approximate depth-averaged river flow velocity of 0.1 m/s. These settings result in an estuary that can be classified as SS (Geyer & MacCready, 2014). Relative to this reference case, we then increase the tidal range and riverine discharge independently to model estuaries characterized by SIPS and SW, respectively. See the bottom two rows of Table 1 for the boundary values chosen for each estuary. The turbulence model parameters are kept constant and are provided in Appendix B2.

Based on the typical dune dimensions observed in the field (see Section 1), our reference dune geometry consists of symmetric dunes with height $H_d = 1.5$ m $(0.1h)$ and length $\lambda_d = 100$ m. Table 2 shows the range of the dune geometry used in this study, which covers the natural range for $h = 15$ m and extends the geometry investigated in the study of Veerapaga et al. (2019) in terms of dune length, asymmetry, and configuration. We consider both ebb- and flood-oriented dunes, in line with field observations (Lefebvre et al., 2022).

Table 2
Estuarine Sand Dune Geometry of the Model Runs for Each of the Respective Estuaries, Sorted by Section

Type of run	# Runs	H_d (m)	λ_d (m)	$\mathcal{A}_d$ (-)	D (-)	Section
No dunes (SW/SS/SIPS)	3	0	-	-	-	§3.1–§3.4
Dune height (SS)	5	✓[a]	100	0	0	§3.2–§3.4
Dune length (SS)	5	1.5	✓[b]	0	0	§3.2
Dune asymmetry (SS)	8	1.5	100	✓[c]	0	§3.2
(Deepening) Dune height (SS)	5	✓[a]	100	0	1	§3.3–§3.4
Dune height and config (SW)	10	✓[a]	100	0	0 and 1	§3.3–§3.4
Dune height and config (SIPS)	10	✓[a]	100	0	0 and 1	§3.3–§3.4

Note. Checkmarks ✓ indicate the variable of interest that is varied across that row of model runs of which the specific parameter values are provided in the table footnotes. [a]Dune heights are $H_d = 0.2$, 0.5, 1.0, 2.5 and 4.5 m. [b]Dune lengths are $\lambda_d = 50$, 70, 100, 200 and 300 m. [c]Asymmetry values are $\mathcal{A}_d = \pm 0.175$, ± 0.350, $\pm$ 0.525 and ± 0.700.

2.4. Model Implementation in Delft3D-FLOW

The estuary model is implemented in Delft3D-FLOW version 4.04 using vertical boundary-fitted σ-coordinates, thus avoiding a step-wise bathymetry (Lesser et al., 2004). For the discretization, a constant horizontal grid cell size of 10 m is used and in the vertical 40 layers are used. The spacing of the lowest 20 layers increases linearly from the bed, with the bottom grid cell height 0.1% of the water depth, or approximately 1.5 cm. This ensures that the bed-adjacent cell center is located within the log layer. The top 20 layers are uniform in height, which leads to a more accurate representation of salt transport compared to retaining the linear increase in these top layers (Appendix C1).

A time step of 2.7 s is used and model output is generated 24 times every tidal cycle over the full domain. Each model simulation is run until a dynamic equilibrium with the tide is attained, characterized by a negligible difference in model output from one tidal cycle to the next. All model runs with a sand dune field ($k_d > 0$) use the output of the flat bed case as initial condition. This ensures that dynamic equilibrium is attained relatively quickly, usually within 120 hr of (simulated) physical time, just shy of 10 tidal cycles. Each model run requires around 20 hr of calculation time on a regular laptop (Intel i7 @2.60 GHz).

A numerical convergence study is performed in the horizontal and vertical directions separately in the reference SS estuary model with dunes of length $\lambda_d = 125$ m. This showed clear convergence in flow velocities, salinity structure, and TKE for subsequent grid refinements in both directions. Similarly, for the system with dune length $\lambda_d = 50$ m, a model with a finer horizontal grid cell size of 5 m was run next to the reference grid cell width of 10 m for a more accurate discretization of the sand dune shape Λ_d, as specified in Equation 3. This grid refinement was found to give a negligible accuracy improvement. More details are provided in Appendix C2.

2.5. Definition of Salt Intrusion Length, Stratification, and Mixing

In this section, the methodology to analyze the salinity structure is presented. First, we introduce averaging operators for a general variable ψ to reduce the variability over 2DV space and time; details on these operators are provided in Appendix D. To denote depth-averaged values of a variable ψ, we use an overbar notation $\overline{\psi}$. Note that, consequently, the depth-integrated value equals $H\overline{\psi}$. Furthermore, the range over at tidal cycle is denoted by $\Delta_t\psi$. The tide-averaged value is denoted by angle brackets $\langle\psi\rangle$, and the spatial average over the entire estuary by square brackets $[\psi]$.

The main focus of this research is the salt intrusion length L_s, which we define as the maximum distance from the seaward side at which the depth-maximum equals the critical concentration of $s_{crit} = 1$ ppt, or

$$L_s(t) = \max_x\left(x \mid \max_z s(x,z,t) \geq s_{crit}\right). \tag{11}$$

This quantity varies over a tidal cycle and we usually refer to the tidally averaged value $\langle L_s\rangle$ when dynamic equilibrium is attained. Furthermore, we consider the region from $x = 0$ to $x = \max_t(L_s)$ as the *Region of Salt Intrusion* (ROSI). For some variables, we are only interested in the behavior in this region. Hence, we define the mean over the ROSI of a variable ϕ with $[\psi]_{ROSI}$ (see Appendix D).

Stratification is defined by $\delta s(x,t) = \max_z(s(x,z,t)) - \min_z(s(x,z,t))$. Since the ratio of stratification and the depth-averaged salinity is often used to describe the vertical salinity structure (Hansen et al., 1966; Valle-Levinson, 2010), we define the stratification parameter as

$$\theta_s(x) = \left\langle \frac{\delta s}{\overline{s}} \right\rangle. \tag{12}$$

When $\theta_s > 1$, the system shows substantial stratification and can locally be classified as a SW. When $\theta_s < 1$, stratification is relatively weaker and the estuary classification ranges from weakly to SS, depending on the relative strength of the estuarine circulation (Valle-Levinson, 2010). To quantify the relative temporal variation in stratification, we use the following:

$$\varphi_s(x) = \frac{\Delta_t(\delta s)}{\langle \delta s\rangle}. \tag{13}$$

When $\varphi_s > 2$, the stratification ranges from highly stratified to well-mixed over the tide. When the temporal variation φ_s is small, stratification is more or less constant over a tidal cycle. Note that we classify and describe the estuary locally on the existing internal salinity structure, rather than an applying overall prognostic estuarine classification based on external forcing parameters (e.g., Geyer & MacCready, 2014).

Finally, we define salinity mixing as the loss of salinity variance due to turbulent mixing (Burchard & Rennau, 2008; MacCready et al., 2018):

$$\mathcal{M}(t) = \int_0^L \int_{z_b(x)}^{\eta(x,t)} 2K_v \left(\frac{\partial s}{\partial z}\right)^2 dz\, dx \tag{14}$$

in ppt^2 m^2/s. Herein, we neglect the horizontal mixing contribution, which is a factor 10^2 smaller than the vertical term due to small horizontal salinity gradients. Note that this simplifies to

$$\mathcal{M}(t) = L[H\overline{\mu}], \tag{15}$$

where $\mu = 2K_v(\partial s/\partial z)^2$ denotes the local mixing in ppt^2/s, which can be evaluated locally. Note that a completely well-mixed system with zero stratification gives $\mathcal{M} = 0$ ppt^2 m^2/s.

3. Results: Influence of Dune Geometry on Salt Intrusion

This section presents the results, specifically focusing on the salinity structure and stratification (Sections 3.1 and 3.4) and the influence of variations in dune geometry on the salt intrusion length (Sections 3.2 and 3.3). Specifically, Section 3.1 visualizes and quantifies the difference in salinity structure between the three estuaries, classifying the estuaries based on the stratification parameters of Section 2.5. Section 3.2 focusses on the influence of sand dune geometry of depth-neutral dunes in the SS system and aims to identify the dominant geometric characteristic influencing salt intrusion. Section 3.3 builds on this and highlights the difference between depth-neutral dunes and deepening dunes for all three estuaries. Finally, Section 3.4 presents how these changes in dune geometry and salt intrusion length are related to the overall hydrodynamics, turbulence, and mixing. An overview of the used model runs in each respective section can be found in Table 2.

3.1. Differences in Salinity Structure for the Three Estuary Types

First, we describe some general model characteristics and highlight the difference in stratification between the three cases. The salinity structure during low and high tide is shown in Figure 2 for each of the three estuary cases without any dunes present. Stratification is larger during low tide, as indicated by elongated isohalines, and the salt intrusion length $L_s(t)$ is near its minimum value. The bottom row of Figure 2 quantifies the salinity structure and stratification. Black lines show the tide- and depth-averaged salinity $\langle \overline{s} \rangle$ and stratification $\langle \delta s \rangle$ in ppt. Purple lines shows the stratification ratio θ_s (Equation 12) and temporal variation in stratification φ_s (Equation 13) along the estuary. In general, we observe that the stratification decreases from SW to SIPS, accompanied by an increase in the salt intrusion length. Furthermore, absolute stratification $\langle \delta s \rangle$ is largest near the salt intrusion limit in each system. The largest relative stratification θ_s is attained near the salt intrusion limit $\langle L_s \rangle$, and shifts landward as mean stratification decreases (SW to SIPS). Below we present the salinity structure of each system.

Salt wedge: The salt intrusion length L_s ranges from 8.4 to 11.2 km over the tidal cycle. Subtidal stratification is largest at the mouth, reaching almost $\langle \delta s \rangle = 30$ ppt. Stratification δs is larger than the depth-averaged salinity throughout the entire estuary, supported by θ_s exceeding unity everywhere. This supports the definition of a SW as defined in Section 2.5. The temporal variation of stratification φ_s increases significantly inland from $x = 8$ km, but this can be attributed to the tidal variation of L_s, rather than a local change in salinity structure over the tidal cycle.

Strongly stratified: The salt intrusion length L_s ranges from 27.3 to 29.3 km over the tidal cycle, this range is smaller to the SW as L_s is located further inland. The relative stratification (θ_s) increases toward the salt intrusion length and exceeds unity halfway the ROSI. Furthermore, the stratification has little variation over the tidal cycle as φ_s approximately equals 0.5 in the ROSI. Stratification is large in general, but θ_s does not exceed unity everywhere and the temporal variation in stratification is small. Therefore, we can classify this system as SS.

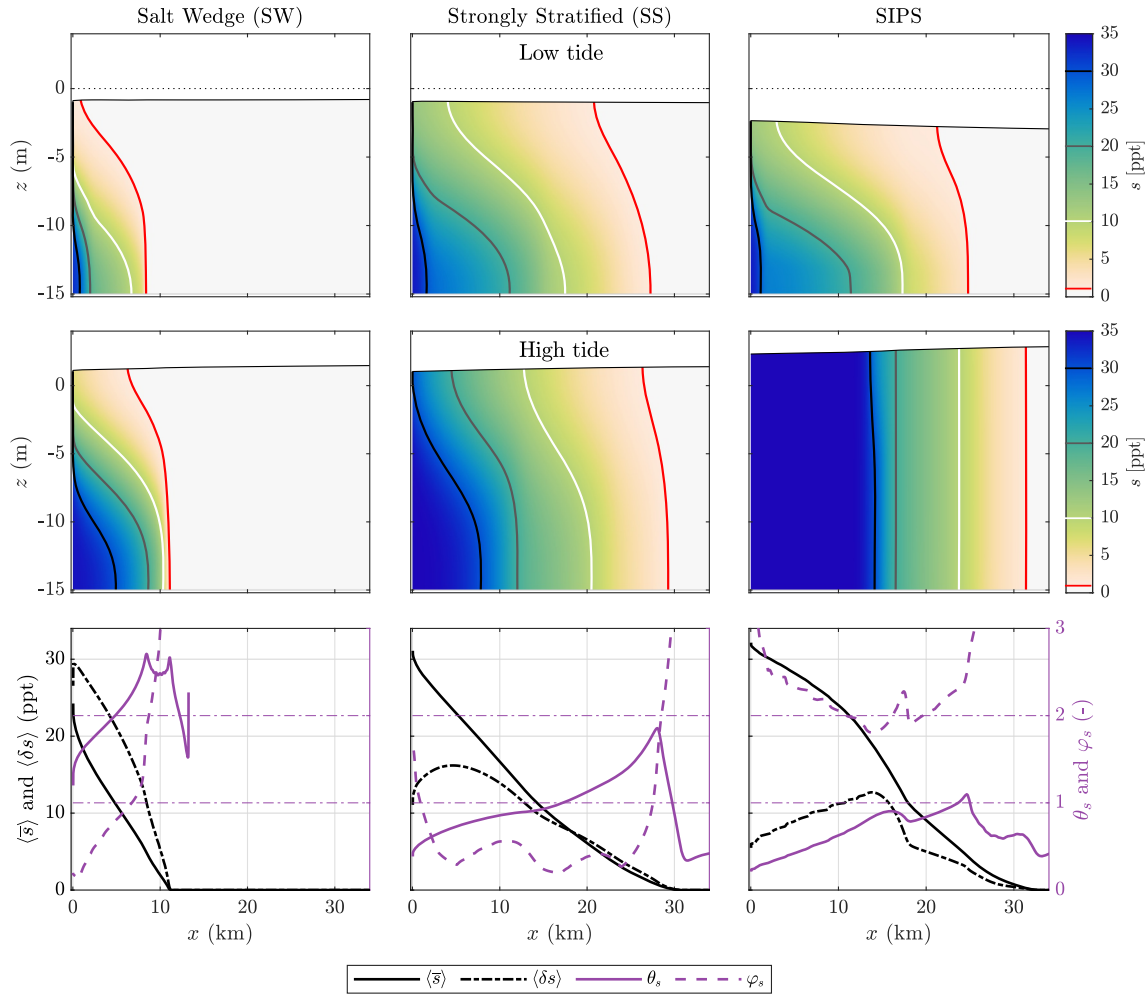

Figure 2. Top and middle: snapshot of salt concentration during low and high tide for all three estuary types, also displaying the free surface elevation. Bottom: salinity and stratification profiles along the estuary. We do not plot up to $x = L = 50$ km, as the shown domain captures the region of salt intrusion for all three estuary cases.

Strain-induced periodic stratification: The salt intrusion length is slightly larger than in the SS system, ranging from 24.7 to 31.7 km, which is a larger range due to the larger tide. Mean relative stratification $\langle\theta_s\rangle$ is smaller compared to previous cases and only exceeds 1 near the salt intrusion limit. Furthermore, the temporal variation in stratification φ_s is large and exceeds 2.0 almost everywhere. This indicates that the system varies from well-mixed to stratified over the tidal cycle, also sketched by the two salinity snapshots in the top and middle figure, resulting in the classification of a SIPS estuary.

The tidal flow velocity decays from the seaward side and equals zero at the riverine boundary. All three systems display some tidal amplification throughout the domain, resulting in approximately 15% more tidal range than specified at the seaward boundary throughout the domain. This amplification is also visible in Figure 2, especially in the SIPS case. This is not unphysical, as tidal amplification occurs in many estuaries worldwide (Khojasteh et al., 2023).

3.2. Influence of Dune Geometry on Salt Intrusion in the Strongly Stratified System

In this section, we quantify the effect of changing dune geometry on the salt intrusion length using depth-neutral dunes as shown in the left of Figure 1c. We only do so for the SS estuary initially, to determine the dominant geometric characteristics. The reference dune field contains symmetric dunes with dune length $\lambda_d = 100$ m and dune height $H_d = 1.5$ m (10% of the water depth). The tidal fluctuations of the depth-maximum salinity $\max_z(s)$ over three tidal cycles in this reference run are shown in Figure 3a, illustrating the dynamic equilibrium and the

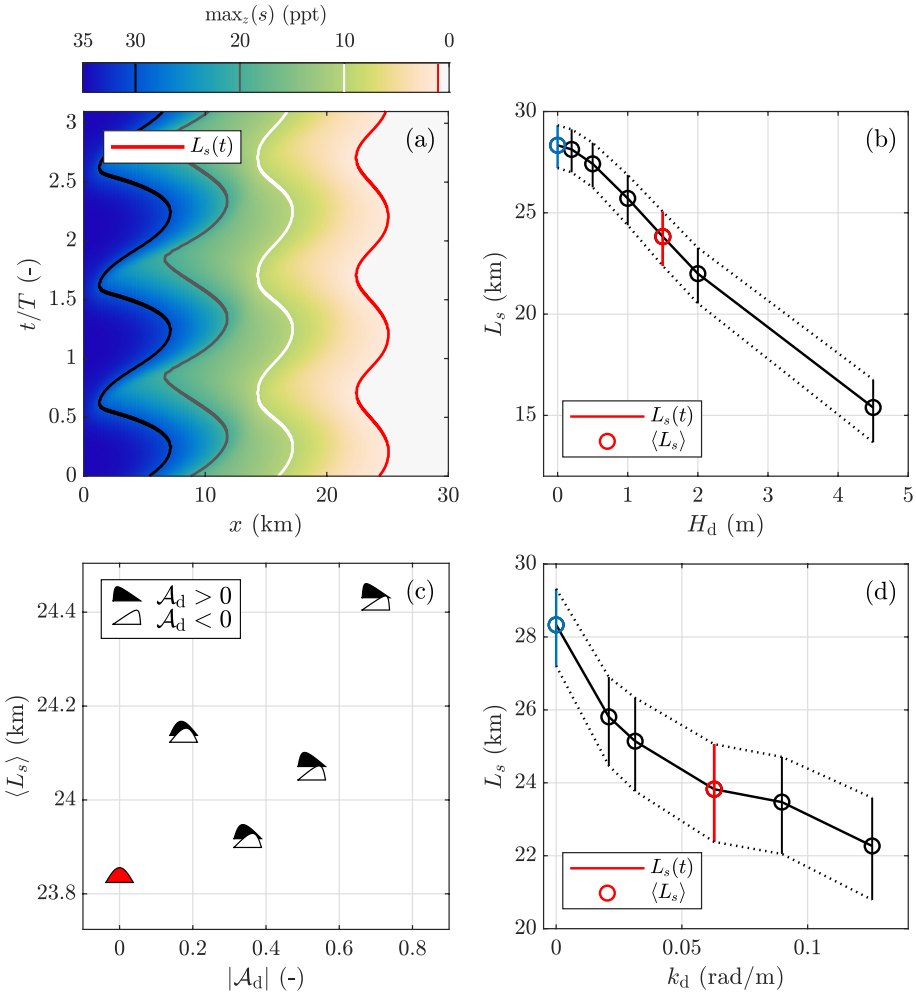

Figure 3. The influence of depth-neutral dune geometry ($D = 0$) on salt intrusion in the strongly stratified estuary. Used parameter values are presented in Table 2. (a) Temporal evolution of the maximum salinity $\max_z(s)$ for the reference dune model with dune height $H_d = 1.5$ m and dune length $\lambda_d = 100$ m. (b) Influence of dune height H_d on salt intrusion length L_s. (c) Influence of dune asymmetry parameter $\mathcal{A}_d$ on subtidal salt intrusion length $\langle L_s \rangle$. (d) Influence of dune wave number $k_d = 2\pi/\lambda_d$ on salt intrusion length L_s. Note the different scales of each axis. The reference dune run is shown in red and the flat bathymetry model run is shown in blue.

horizontal excursion of the salt intrusion length $L_s(t)$ throughout the tidal cycle. Changes in dune geometry for depth-neutral dunes ($D = 0$) are applied relative to the reference case while varying a single dune geometry parameter. Figure 3 shows the influence of changing dune height H_d (panel b), dune asymmetry $\mathcal{A}_d$ (panel c) and dune length (panel d, by means of wavenumber $k_d = 2\pi/\lambda_d$), on the salt intrusion length L_s . The red vertical line in Figures 3b and 3d indicates the tidal variation of L_s in the reference model run as in Figure 3a. The blue marker indicates the flat bed run, equivalent to both $H_d = 0$ m and $k_d = 0$ rad/m.

Within the tested parameter space, the largest changes in salt intrusion $\langle L_s \rangle$ occur by varying the dune height; steeper (higher and shorter) dunes decrease salt intrusion by several kilometers, indicated by the influence of dune height H_d and dune wavenumber k_d. These results are similar to Veerapaga et al. (2019). The influence of dune height appears to behave linearly in the middle of the tested parameter space. The influence of dune length (or dune wavenumber) is nonlinear.

The influence of dune asymmetry is smaller than dune length and height. Generally, in this hydrostatic model, salt intrusion increases with increased asymmetry. Interestingly, ebb-oriented dunes ($\mathcal{A}_d > 0$) always show slightly more salt intrusion than their flood-oriented equivalents ($\mathcal{A}_d < 0$). However, this difference is small (single grid cell width) and might be the consequence of numerical inaccuracies. More importantly, the small difference

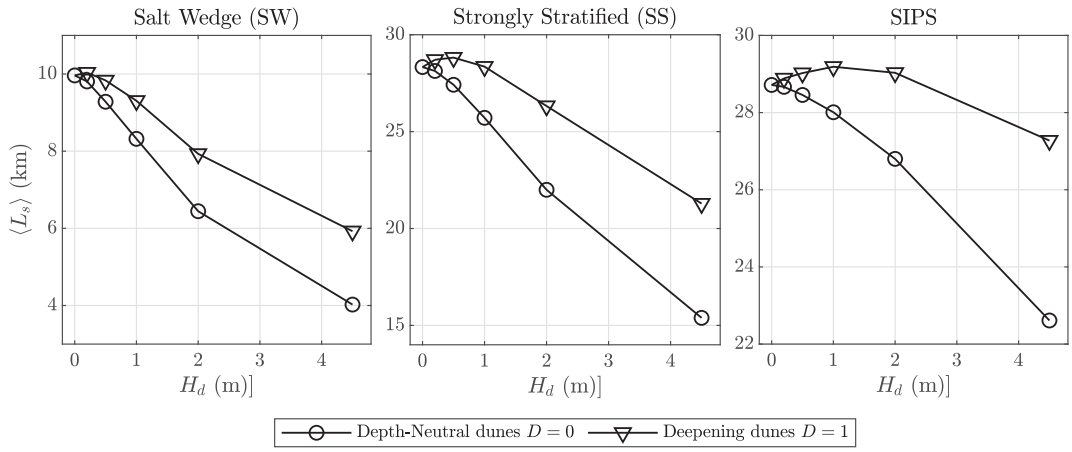

Figure 4. Influence of dune height H_d of both depth-neutral dunes ($D = 0$) and deepening dunes ($D = 1$) on subtidal salt intrusion length $\langle L_s \rangle$ for each estuary type.

between ebb- and flood-oriented dunes indicates that these results might rely on the discretization and bed characteristics, rather than turbulent structure.

3.3. The Effect of Dune Height Across Different Estuaries

Next, we determine the influence of deepening dunes as on the right of Figure 1c. The results in Section 3.2 have indicated that dune height is the dominant factor of salt intrusion length for depth-neutral dunes within the examined geometry parameter space (Table 2). Therefore, in the case of deepening dunes ($D = 1$), we only examine the influence of dune height H_d while fixing the symmetry $\mathcal{A}_d = 0$ and dune length $\lambda_d = 100$ m.

The influence of dune height for each of the three estuaries is shown in Figure 4. In all three cases, dunes that maintain mean depth ($D = 0$) monotonically decrease salt intrusion with increased dune height by several kilometers. However, in the case of deepening dunes, salt intrusion is increased when dunes are only small. The mitigating effect of increased dune height on salt intrusion is counteracted by the increase in water depth, which increases salt intrusion (when no regime shifts occur). When the deepened dune height is increased further, the salt intrusion length decreases by several kilometers compared to the initially flat bed cases. The transition where a system with deepening dunes produces a salt intrusion length $\langle L_s \rangle$ less than the flat bed case occurs at approximately $H_d = 0.3$, 1.1, and 2.4 m for our SW, SS, and SIPS-cases, respectively.

With increasing stratification (from SIPS to SW), deepening estuarine sand dunes appear to become more effective in generating additional mixing to reduce salt intrusion. In the SIPS case, dunes higher than 1.5 m (10% of the water depth) are required to reduce $\langle L_s \rangle$.

3.4. Changes in Hydrodynamics, Turbulence, and Mixing

Finally, we show the changes in hydrodynamic characteristics and turbulence resulting from variations in dune height H_d—as used in Section 3.3—to explain how salt intrusion is reduced. Figure 5 illustrates the estuarine mean of the subtidal value $[\langle \cdot \rangle]$, and range over the tide $\Delta_t \cdot$ of the depth-averaged flow velocity $\overline{u}$ and the free surface elevation η. Velocity scales are normalized by the estimates of the depth-averaged river flow velocity and depth-averaged tidal flow velocity amplitude (as in Hendrickx et al., 2023), defined by

$$U_r = -\frac{q_{river}}{h} \quad \text{and} \quad U_t = A_{sea}\sqrt{\frac{g}{2h}}, \tag{16}$$

respectively. The mean tidal range along the estuary is normalized by the seaward tidal range $2A_{sea}$.

The top row of Figure 5 displays the mean subtidal depth-averaged flow $[\langle \overline{u} \rangle]$, which reflects the mean river flow velocity. It is worth noting that, the mean flow remains more or less constant for increasing depth-neutral dune

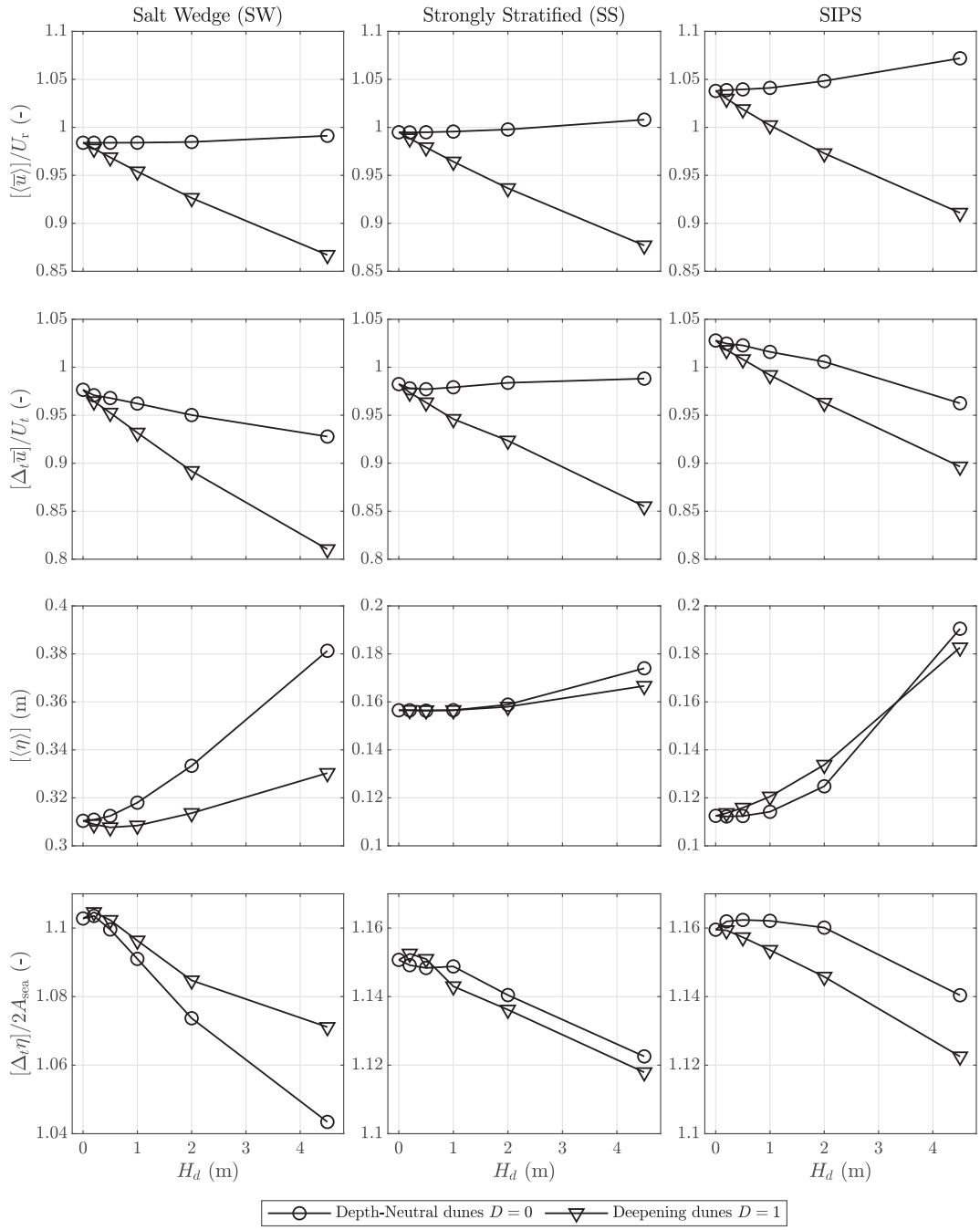

Figure 5. Normalized values of the estuarine mean of the subtidal value $[\langle \cdot \rangle]$ and tidal range $[\Delta_t \cdot]$ of the depth-averaged horizontal flow velocity $\overline{u}$ and free surface elevation η for varying dune height. Mean-free surface elevation $[\langle \eta \rangle]$ (third row) is not nondimensionalized.

height, but decreases in magnitude with larger deepening dunes. This suggests that the river flow is not significantly affected by bedform drag, but is instead more responsive to changes in mean bed elevation.

The second row shows the mean tidal range of the depth-averaged flow velocity $[\Delta_t \overline{u}]$, representing tidal flow velocities. The response to deepening dune height is similar to the change in mean river flow velocity and is attributed to changing mean bed levels. However, in contrast to the mean flow, tidal velocities decrease with increasing depth-neutral dune height (up to 10% for the largest dunes) in the SW and SIPS estuaries. Form

roughness causes additional drag to the flow, causing deceleration in the flow for the depth-neutral dunes. Deepening dunes cause deceleration, by both this form drag and deepening of the system.

This reduction in tidal flow is accompanied by a rise in mean water levels, as shown in the third row, again especially in the SW and SIPS system. Water levels change relatively little in the SS system. The diminishing difference between deepening and depth-neutral dunes is of particular interest, which even reverses when stratification weakens (i.e., the change in the order of $-\bigtriangledown-$ and $-\bigcirc-$ moving from SW to SIPS). In the SIPS estuary, the influence of deepening dunes on mean water levels is equally strong to the influence of depth-neutral dunes, even though flow velocities are decreased more.

This reversal also applies to the mean tidal range $[\Delta_t \eta]$ (fourth row). In the SS system, depth-neutral dunes reduce the tidal range more strongly, whereas the opposite is true for the SIPS system. Furthermore, small depth-neutral dunes even slightly increase the tidal range in the SIPS system.

Overall, based on decreased flow velocities and mean tidal amplitude, we see an effect of form roughness on the tidal flow, which is both observed and modeled for estuarine sand dunes and attributed to flow separation (Lefebvre et al., 2011, 2014; Lefebvre & Winter 2016). However, it is important to note that nonhydrostatic processes are not necessary for this effect to occur, similar to the findings of Portos-Amill et al. (2024).

Figure 6 presents various nondimensionalized turbulent and mixing characteristics for varying dune height. Specifically, the mean magnitude of the bed shear stress $[\langle|\tau_b|\rangle]_{\mathrm{ROSI}}$, depth-integrated TKE $\left[\langle H\bar{k}\rangle\right]_{\mathrm{ROSI}}$, the mean depth-averaged eddy diffusivity $\left[\langle\overline{K_v}\rangle\right]_{\mathrm{ROSI}}$, the mean stratification $[\langle\delta s\rangle]_{\mathrm{ROSI}}$ and the overall mixing of the system $\langle\mathcal{M}\rangle$. Note that higher TKE generally indicates greater diffusivity, leading to increased mixing. Stratification inhibits turbulence and the TKE and diffusivity are an order of magnitude larger in the freshwater region. Consequently, these quantities' estuarine mean $[\,\cdot\,]$ is inversely proportional to L_s. Therefore, we have taken the ROSI-mean $[\,\cdot\,]_{\mathrm{ROSI}}$ of these turbulent quantities to determine the influence of dune height on salt dynamics. Normalization is applied with the characteristic flow velocity $U = |U_r| + U_t$, a freshwater density $\rho_0 = \rho(s_{\mathrm{river}})$. Normalization of mixing $\mathcal{M}$ is done by $M = s_{\mathrm{sea}}^2 hL\omega$ (see Appendix E).

The top row of Figure 6 shows how the bed shear stress magnitude increases in all three systems for depth-neutral dunes. The relationship with deepening dune height depends on the system; bed shear stress increases in the SW system, whereas it decreases in the SIPS system.

The second row shows that larger dunes increase the TKE, particularly for depth-neutral dunes. The change in TKE is relatively larger for the SW system as stratification decreases most. Deepening dunes initially decrease TKE for small dune heights and only cause a rise in TKE when they are sufficiently high, a pattern similar to the reduction in salt intrusion length observed in Figure 4. In general, a higher bed shear stress means more generation of TKE. Therefore, the SIPS system reveals that the increase in TKE is also influenced by other factors; despite a decrease in bed shear stress, TKE increases with larger deepening dunes. Furthermore, flow velocities decreased with these larger dunes (Figure 5). This indicates that the sand dune shape creates additional turbulence.

As shown in the third row, the vertical diffusivity K_v reproduces the pattern of the TKE, although deepening dunes increase diffusivity at an earlier stage compared to TKE. The patterns of these first three quantities—bed shear stress, turbulence, and diffusivity—exhibit a relationship qualitatively similar to the influence of dune height H_d on the salt intrusion length $\langle L_s\rangle$ as depicted in Figure 4. Depth-neutral dunes directly increase these variables, thus decreasing salt intrusion. Deepening dunes only increase these characteristics compared to the flat-bed case when dunes are sufficiently large. Again, this occurs for less high dunes in the SW case, higher dunes are needed in the SIPS system to cause this effect.

The fourth row shows that larger dunes decrease stratification. This effect is strongest in the SW case, in which the mean stratification decreases more than 25%. Salinity responses are less strong in the SS and SIPS cases, where initial mean stratification is lower. For the SS case, the change in stratification is equal for depth-neutral and deepening dune height, whereas deepening dunes decrease stratification more in the SW and SIPS cases.

The bottom row shows how the decrease in stratification reduces the total mixing $\mathcal{M}$ in the system. This effect is especially notable in the SIPS system, where the two lines nearly overlap, despite differences in stratification $[\langle\delta s\rangle]_{\mathrm{ROSI}}$. The mixing in the SS and SIPS systems is very similar, mixing in the SW system is larger, mostly due to more stratification. Strikingly, mixing appears to strongly correlate with dune height H_d for both dune types,

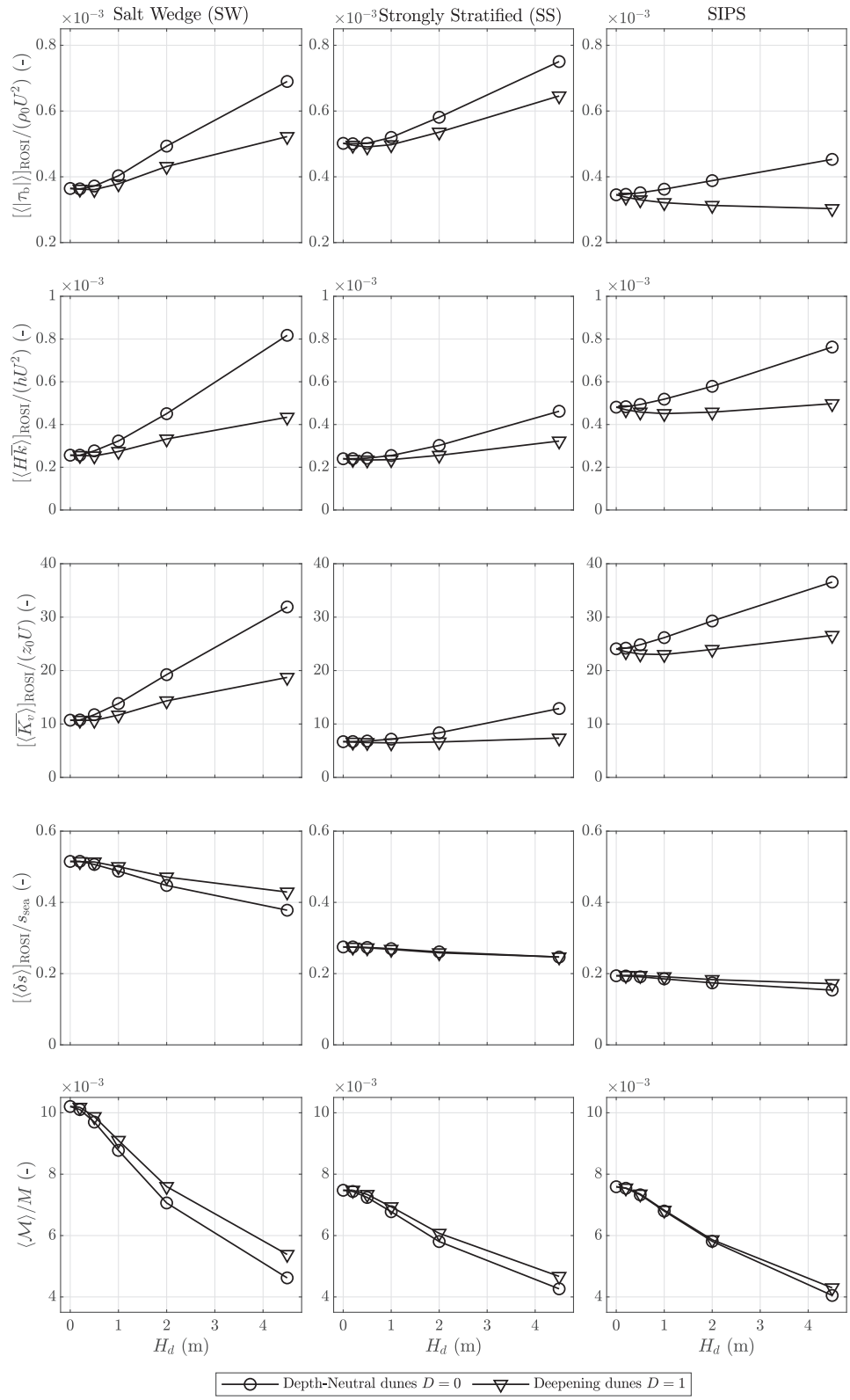

Figure 6. Normalized values of the region of salt intrusion mean of the subtidal value $[\langle \cdot \rangle]_{\mathrm{ROSI}}$ of the bed shear stress magnitude $|\tau_b|$, depth-integrated turbulent kinetic energy $H\bar{k}$ (second row), depth-averaged vertical diffusivity $\overline{K_v}$ (middle row), stratification δs (fourth row). The bottom row shows the subtidal mixing $\langle \mathcal{M} \rangle$ in the entire estuary. Vertical axes are normalized, see Appendix E for motivation.

suggesting that in these systems, mixing depends primarily on dune height and not on the salt intrusion length $\langle L_s \rangle$. The mean depth changes caused by deepening dunes do not alter this relationship. Overall, mixing $\mathcal{M}$ decreases as the salinity structure adjusts and stratification is reduced. Given the discrepancy of bed shear stress and turbulence, and the strong correlation of $\mathcal{M}$ with H_d (rather than $\langle L_s \rangle$), we attribute this effect to the shape of the sand dune itself.

All in all, the above analysis suggests that several mechanisms contribute to reducing salt intrusion. For depth-neutral dunes, larger dunes reduce the tidal flow and tidal amplitude due to increased flow roughness. The river flow velocity is largely unaffected by this form roughness and remains a function of the mean water depth, resulting in equal seaward flushing. The sand dune shape increases turbulence and diffusivity, by processes more than bed shear stress alone, which enhances local mixing. Hence, the salt intrusion length decreases and the total mixing quantified by $\mathcal{M}$ decreases as stratification is reduced.

For deepening dunes, riverine flushing decreases linearly with increased dune height (top row of Figure 5), increasing salt intrusion. At the same time, tidal flow velocities decrease, both by changing mean water depth and by form roughness. However, for a sufficiently large dune height, sufficient vertical mixing by turbulence is generated to counteract this effect and reduce salt intrusion overall. In a system with significant stratification, this critical dune height that causes increased turbulent mixing is smaller than in a system that already has relatively little stratification.

4. Discussion

In Sections 4.1 and 4.2, we discuss some of the model assumptions and modeling choices and how they potentially affect model outcomes. Next, we highlight some local processes over individual dunes to show how turbulent mixing is enhanced in Section 4.3. Finally, Section 4.4 discusses the practical implications of this research for mitigating salt intrusion, highlighting the link between dunes and dredging activities.

4.1. Model Geometry and Set-Up

The advantage of the idealized model setting is that it allows us to trace changes in salt intrusion length directly back to dune characteristics. The influence of lateral processes, depth and width convergence, and multi-channel systems is excluded, and these effects are considered next.

We have assumed an estuary of relatively narrow width with little lateral variation, justifying the use of a 2DV estuarine model that captures the importance of horizontal and vertical salinity gradients in estuaries (MacCready & Geyer, 2010; Valle-Levinson, 2010). The model also incorporates a sand dune geometry that has relatively uniform lateral geometry (Bradley et al., 2013; Hulscher & Dohmen-Janssen, 2005; Lefebvre et al., 2022; Zorndt et al., 2011). However, the influence of lateral processes in wide estuaries and multi-channel systems on salt transport are neglected (Biemond et al., 2023). Furthermore, the assumption of a uniform width leads to a spatially uniform background river velocity along the estuary, whereas many estuaries have a funnel-like shape, resulting in spatial variability of the river velocity and various types of tidal propagation (Khojasteh et al., 2023). The average bed level is a schematization of the seaward part of the RWW only, and neglects a bed slope and changing mean water depth toward the inland regions. These factors collectively influence the overall river flow velocity and tidal (vertical) mixing, both key predictors of salt intrusion (Geyer & MacCready, 2014; Hendrickx et al., 2023).

The estuary length $L = 50$ km is a physical characteristic of the system, representing the length over which the tidal influence attenuates, and is sufficiently large to capture the salt dynamics. The sensitivity of salt intrusion to the estuary length is marginal; the intrusion length rises by about 1 km only when using $L = 200$ km instead of 50 km in the SS estuary.

4.2. Model Implementation, Hydrostatic Assumption, and Turbulence Closure

Vertical boundary-fitted σ-coordinates are selected for discretization in this study. Although a Cartesian grid may offer better accuracy for salt dynamics over steep topography (Bijvelds, 2001; Stelling & van Kester, 1994), it is considered impractical due to model requirements and computational limitations. Achieving an accurate representation of the near-bed flow and turbulent effects necessitates small vertical grid cell sizes (of around 1.5 cm) near the bed. When a Cartesian grid is developed with this model requirement in mind, many grid cells (100–300

layers) are required to model the highest dunes. With the used discretization, we acknowledge that the condition for "hydrostatic consistency" (Deltares, 2024; Haney, 1991) is violated in the bottom cells. However, this influence is small, as a hydrostatical consistent discretization with a cell width of 1.25 m produces equal results (Appendix C2). The absence of a global bed slope allows for precise spatial discretization of the estuarine sand dune shape while maintaining a bottom cell center positioned within the log-layer of the wall function, without increasing computational cost. The model shows good numerical convergence and the numerical error due to the grid is small (Appendix C2).

The hydrostatic assumption is valid as the vertical accelerations in the flow are an order 10^2 smaller than the gravitational acceleration. On a more practical note, the nonhydrostatic module of Delft3D-FLOW requires a Cartesian grid, which is an unfeasible model choice for sand dunes as described above. The hydrostatic assumption aids the computational efficiency and the model performs well with low-angled sand dunes. However, the exclusion of nonhydrostatic processes such as internal wave-breaking (Pietrzak & Labeur, 2004) and flow separation for steep dunes (Lefebvre & Winter 2016) potentially leads to an underestimation of turbulent diffusivity. Employing a nonhydrostatic model would likely result in a larger reduction of salt intrusion with increased dune aspect ratio H_d/λ_d. Therefore, the mitigating effect of sand dunes on salt intrusion may be even greater than currently anticipated.

Constant background turbulence values (Appendix B2) ensure realistic turbulent dispersion throughout the domain. Their values are derived from the nondimensional parameters in the modeling study of Dijkstra et al. (2022). The effect of turbulence suppression by stratification (Geyer, 1993) is also modeled within the k-ϵ model (Deltares, 2024). However, when the influence of processes such as vortex shedding (Best et al., 2001; Bradley et al., 2013) and internal wave breaking (Pietrzak et al., 1991) is of interest, a more accurate representation of turbulence might be required to solve the intricate turbulence processes over sand dunes. Currently, the RANS equations employed here within the Delft3D-FLOW software capture the local and temporal variation of the turbulence due to bed shear stress and internal shear, but neglect such transient flow patterns (Ciofalo, 2022). An LES model that resolves more of the small-scale turbulence might be required for including time-dependency and further resolution of spatial structures, potentially enhancing understanding (Geurts, 2022).

4.3. Increased Turbulent Diffusivity With Sand Dune Height and Mixing Over a Tidal Cycle

In this section, we discuss the qualitative difference in turbulent structures over sand dunes. Figure 7 shows the vertical eddy diffusivity K_v over sand dunes at a fixed location in the estuary around $x = 15$ km for four different dune configurations. This is shown at peak flood, when the eddy diffusivity is largest near the bed. Note that this is for illustration purposes; a fixed estuarine position x cannot be used to compare different models quantitatively. With different models, the salt intrusion length changes, meaning that the salinity structure and turbulence differ for a fixed position x. Alternatively, when comparing models at a location with equal salinity structure (i.e., on $\overline{s}$), the tidal velocity differs. This ambiguity is the reason we have focused on mean processes so far and only discuss qualitative differences in this section.

Figure 7 illustrates how larger dunes induce larger eddy diffusivity in the water column, significantly larger than the constant background values. These are local effects, in line with the topography, and generated by the shear of the flow with the inclined bed. For the large dunes ($H_d = 2.0$ m), depth-neutral dunes induce more turbulent mixing than deepening dunes at this location. For the deepening dunes, the system has a significantly larger volume, causing a decrease in river flow velocities (Figure 5). Simultaneously, the tidal flow velocity and amplitude is decreased, reducing turbulence generation (Figure 6). In Figure 7, the opposite is true for the smaller dunes of height $H_d = 0.2$ m, where deepening dunes have a larger eddy diffusivity at this specific location. This is an effect of the ambiguity issue described above, as the overall mean eddy diffusivity is always larger for depth-neutral dunes for a given dune height (Figure 6).

The eddy diffusivity K_v is not directly representative for mixing μ as used in Equation 15. The local salinity mixing μ is shown at eight moments during the tide for two different depth-neutral dune configurations with dune heights $H_d = 0.2$ m and 2.0 m in Figures 8 and 9, respectively. The free surface elevation η is specified in each moment in time, depicting the stage in tidal cycle. The depth-averaged flow velocity $\overline{u}$ includes both the river and tidal flow velocity.

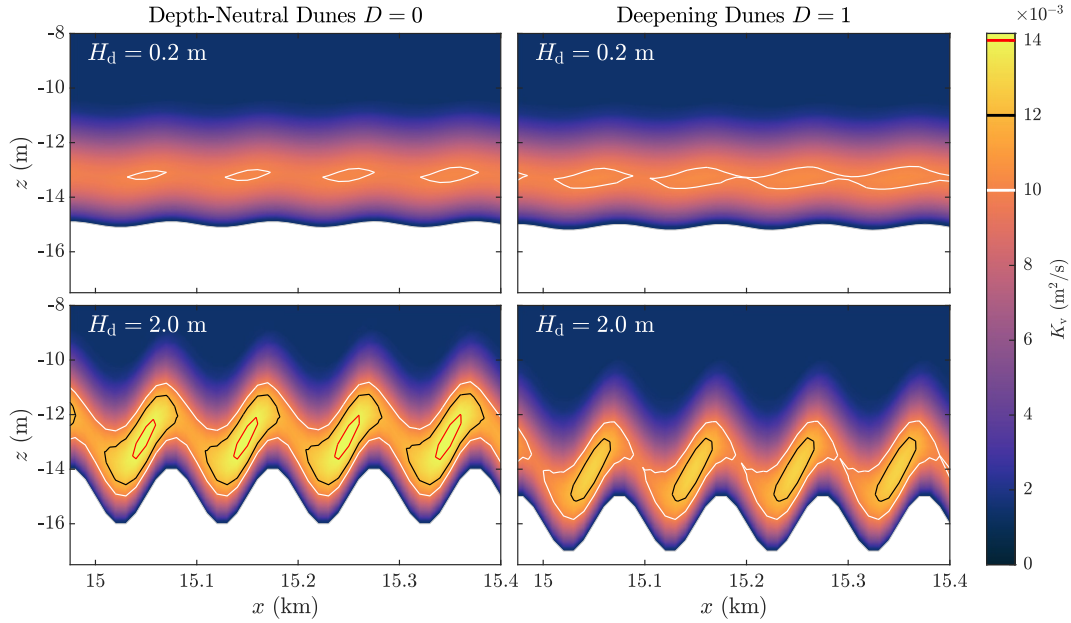

Figure 7. Vertical eddy diffusivity over individual dunes during peak flood tide with four different dune types in the strongly stratified model. The colored contour lines are meant for visualization purposes, indicating the levels of $K_v = 10 \cdot 10^{-3}$, $12 \cdot 10^{-3}$, and $14 \cdot 10^{-3}$ m^2/s, as also depicted in the colorbar.

Both Figures 8 and 9 show that mixing μ is larger in the water column than near the bed, even though the diffusivity is smaller in the upper water column (Figure 7). Vertical salinity gradients are larger in the upper water column and the system is relatively well-mixed near the bed. Furthermore, mixing is generally larger during ebb than during flood, due to an increase in stratification as isohalines elongate during ebb (Figure 2).

During ebb, mixing within the troughs of the dunes is smaller than above the crests and there is relatively little local variation in mixing over the topography. Especially for the small sand dunes of Figure 8, little local variation of mixing can be seen during ebb. For the larger sand dunes of Figure 9, mixing seems to be inhibited in the troughs during slack tide when flow reversal occurs (top-left).

During flood, there is increased mixing at the stoss side (as defined relative to the river flow direction, see Figure 1) of the dunes. This is observed in both small and large dunes, but the magnitude of this effect is much more significant for the larger sand dunes in Figure 9. This local mixing in the troughs is caused by turbulence and exceeds mixing just above the bedforms. Again, note how this peak in local mixing is not necessarily in line with the maximum eddy diffusivity that occurs on the lee side of the sand dunes during flood.

All in all, sand dunes locally increase eddy diffusivity, proportional to a change in dune height. Mixing is strongest during ebb, and local changes of sand dunes on vertical mixing are mostly present during flood.

4.4. Estuarine Sand Dunes as a Nature-Based Solution

This study presents three types of estuaries with various degrees of stratification, ranging from a SW to a SIPS estuary, regulated by the boundary conditions (Geyer & MacCready, 2014). Each estuary classification is not changed by changing the dune geometry. Although the mean depth changes (by 15% maximum), the dominant processes persist and the flow patterns do not change qualitatively. These findings are similar to those by Ralston and Geyer (2019), who observed that dominant means of estuarine exchange are not changed after lowered bed levels by dredging in the Hudson estuary; depth changes were compensated by the adaptation of the along-estuary salinity gradient. Note that this only holds as depth changes are relatively small such that no regime shift occurs (Dijkstra et al., 2022).

This study shows that sand dunes mitigate salt intrusion for the modeled stratified systems, but their effectiveness varies across the different estuarine systems. How this behaves outside of the examined estuaries is unclear. Examples include well-mixed estuaries, estuaries with large lateral variation or meandering estuaries, which are

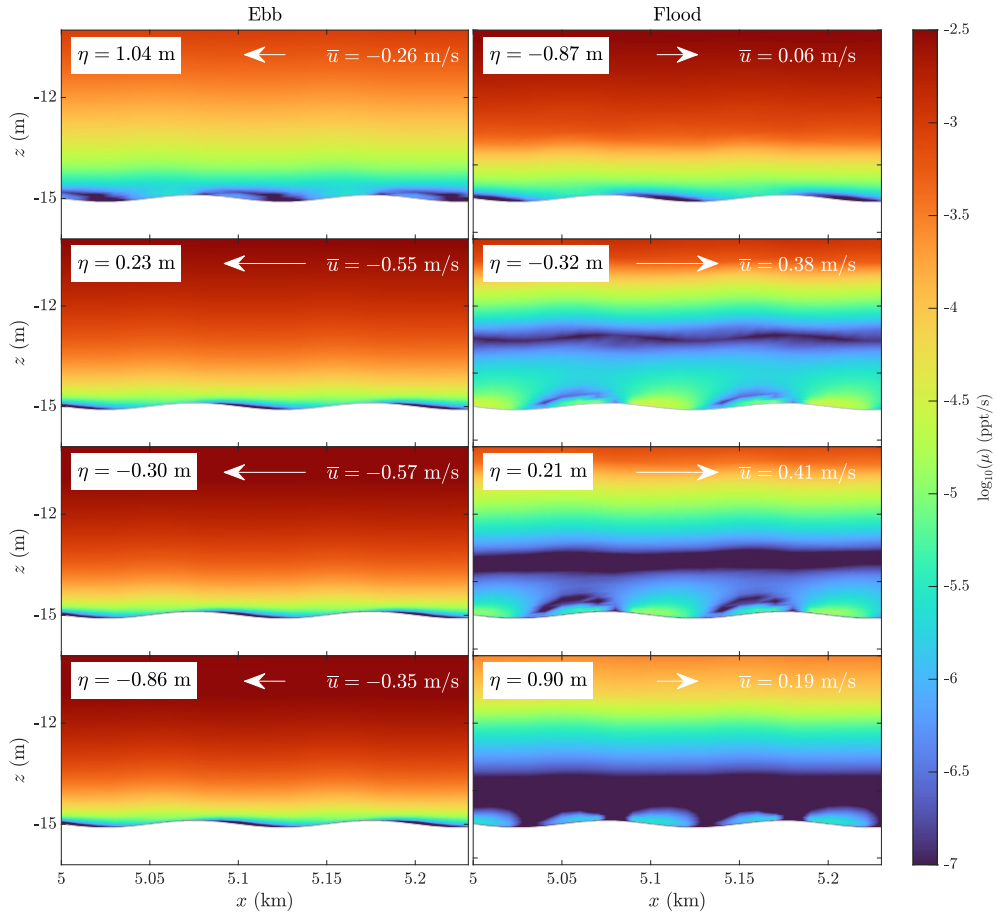

Figure 8. Local mixing coefficient μ (Equation 15, in logarithmic scale) at different moments of the tide over dunes with height $H_d = 0.2$ m, at different moments during the tide. The left column shows four moments during ebb, right column four moments during flood. For every snapshot, the local free surface elevation η and local depth-averaged flow velocity $\overline{u}$ are given at $x = 5.1$ km, where the bed level is equal to the reference level $z_b = -h$. White arrows are for visualization purpose of the flow direction.

not covered by this study. Moreover, salt intrusion is most detrimental during extreme events, in particular low river discharges and storm set-ups. Mitigating measures that rely on an increase of vertical mixing are less effective during set-up events (Kranenburg et al., 2022). To investigate the influence of sand dunes in real-world estuaries, more complex realistic 3D models should incorporate these bedforms. To aid the computational efficiency, a form roughness parameterization (as in Portos-Amill et al., 2024) that captures the influence of sand dune geometry on salt dynamics can be employed. Alternatively, a parametrization that relies on the momentum balance can be considered when investigating less stratified estuaries (Bo & Ralston, 2020).

The change in salt intrusion length is in the order of several kilometers for the highest dunes. External estuarine-scale factors, such as tidal amplitude and river flushing, influence the salt intrusion length to a larger degree (also indicated by the SW case compared to the SS case with increased river flow). However, these processes are under limited human control: flow can be diverted over the different branches but the total discharge remains the same. Estuarine meanders can be created and the average water depth could be decreased, but such measures are often unfeasible due to existing infrastructure along the estuary and the required navigation depth for shipping. When bedforms are not deliberately altered, sand dunes tend to exist in estuaries. This study illustrates that dunes enhance turbulence and mixing and reduce salt intrusion, mainly determined by dune height and steepness. Deepening dunes can do so as well while maintaining navigability. We have shown that salt intrusion can be reduced several kilometers, even though the mean depth is increased. Besides the mitigating potential, the results suggest that classical dredging operations may be unfavorable to salt intrusion issues. The influence of dune height H_d of depth-neutral dunes shows that bed-leveling procedures that decrease H_d, such as the "swiping"

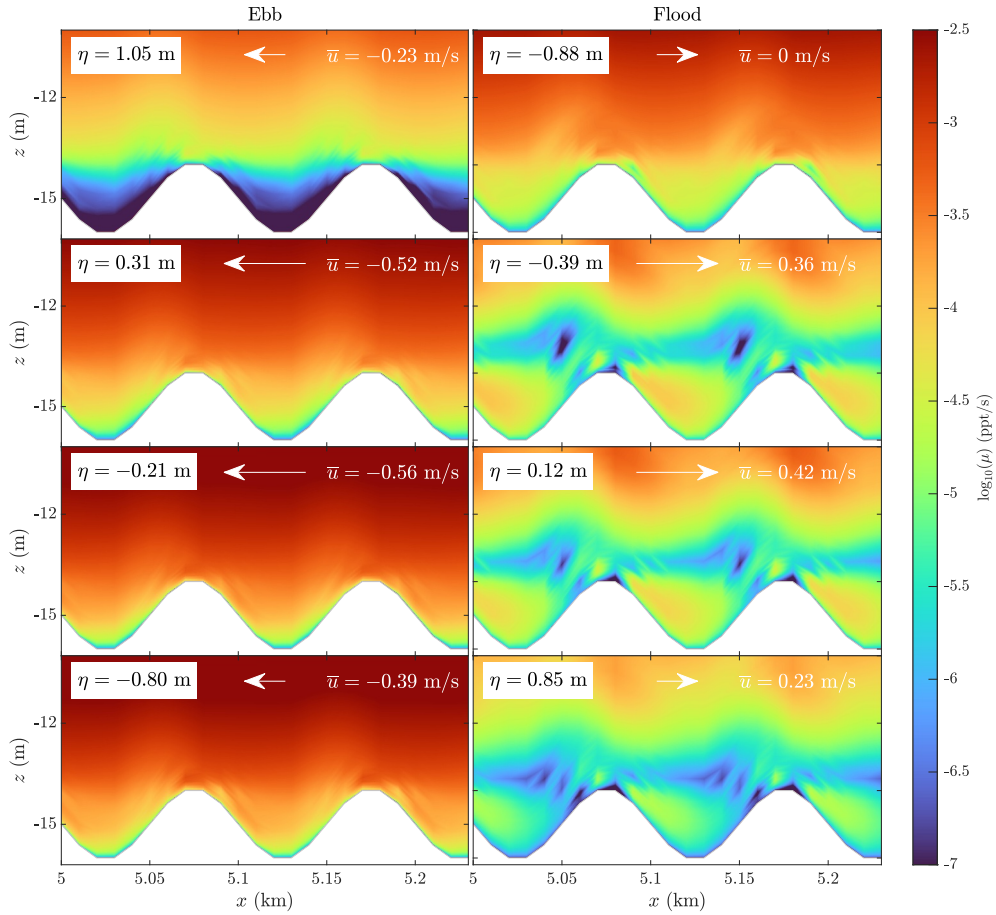

Figure 9. Local mixing coefficient μ (Equation 15, in logarithmic scale) at different moments of the tide over individual dunes with height $H_d = 2.0$ m, at different moments during the tide. The left column shows four moments during ebb, right column four moments during flood. For every snapshot, the local free surface elevation η and local depth-averaged flow velocity $\overline{u}$ are given at $x = 5.1$ km, where the bed level is equal to the reference level $z_b = -h$. The white arrows are for visualization purposes of the flow direction.

method (Campmans et al., 2021), tend to increase salt intrusion. This highlights the importance of preserving an undulating topography (possibly by bedforms) that facilitates mixing and limits salt intrusion.

This research especially focuses on the influence of a morphostatic bathymetry. To optimize mitigation strategies, it is crucial to evaluate the equilibrium shapes of dunes in specific estuarine contexts. Future studies should also include the morphodynamic evolution of sand dunes, and include processes such as salinity gradients (van der Sande et al., 2021; van der Sande et al., 2023), the role of worms and benthic organisms (Damveld et al., 2019, 2020) and fine sediments near the estuarine turbidity maximum (Cheng et al., 2022). Ensuring that designed dune shape characteristics align close to the system's natural equilibrium minimizes the need for frequent dredging activities. This reduces human intervention and maximizes the natural efficacy. As adaptable and dynamic measures, estuarine sand dunes present a nature-based solution with significant potential to mitigate salt intrusion in estuarine environments.

5. Conclusion

We have investigated the influence of estuarine sand dunes on the salinity structure and changes in hydrodynamics and turbulence. We focused on a single-channel estuary with uniform geometry with three types of external forcing, and dynamically resolved flow velocities, salt transport and free surface elevation. Turbulence was modeled locally. Models with different bathymetry are run until a dynamic equilibrium of the salinity structure with the tide was attained. This approach allowed us to examine the relation between salt intrusion and

dune geometry exclusively across different stratified estuaries. A large part of a realistic dune geometry parameter space was systematically explored to determine the dominant bathymetry features influencing salt intrusion.

This research underlines the significance of considering estuarine sand dunes when determining salt intrusion with a numerical model. Changes in dune geometry may significantly impact the salt intrusion length. The examined dune geometry parameter space does not include settings that would change the overall estuarine and transport classification for each of the three estuary types; qualitatively, the dominant mechanisms did not change. Quantitatively, differences occur in the hydrodynamics and mixing that cause a change in the salinity structure. In general, mixing is increased with higher dunes in stratified estuaries, reducing salt intrusion. This effect is strongest when the initial stratification of the flat-bed system is larger.

The potential to reduce salt intrusion via bedform manipulation highlights the importance of having these bedforms in systems where salt intrusion is problematic and emphasizes the adverse effects associated with dredging. Dredging, and taking sediment out of the system, increases the mean water depth and removes naturally occurring bedforms, resulting in increased salt intrusion. Concurrently, this research demonstrates the potential of developing efficient dredging strategies, that retain vertical variation of the bed (such as artificial bedforms) while maintaining navigability. A sufficiently deep dredged dune pattern can generate sufficient vertical mixing to counteract the increased salt intrusion that results from channel deepening. Given that these bedforms are naturally present or tend to develop, estuarine sand dunes can likely serve and be used as a nature-based solution to mitigate salt intrusion.

Appendix A: Envelope Function for Dune Field Placement

The envelope function, describing the location of the dune field in Equation 2, reads

$$b(x) = \frac{1}{1 + \exp\left(-4 \cdot \frac{x - L_0}{\Delta L_0}\right)} + \frac{1}{1 + \exp\left(-4 \cdot \frac{L - x - L_0}{\Delta L_0}\right)} - 1, \tag{A1}$$

where we use spacing parameter $L_0 = 800$ m and envelope ramping parameter $\Delta L_0 = 400$ m.

Appendix B: Turbulence Modeling in Delft3D-FLOW

The turbulent eddy viscosity is determined by $\nu_{3D} = c_\mu k^2/\epsilon$ for constant $c_\mu = 0.09$. The value of ν_{3D} is determined by the k-ϵ turbulence closure, which models the TKE k and energy dissipation ϵ by two coupled nonlinear transport equations, further explained in Appendix B1. How this feeds back into the flow and transport equations is presented in Appendix B2.

B1. Turbulence Closure Equations

The TKE k and dissipation ϵ are modeled by two nonlinearly coupled transport equations, given by

$$\frac{\partial k}{\partial t} + u\frac{\partial k}{\partial x} + w\frac{\partial k}{\partial z} = \frac{\partial}{\partial z}\left(D_k \frac{\partial k}{\partial z}\right) + P_k + B_k - \epsilon, \tag{B1}$$

$$\frac{\partial \epsilon}{\partial t} + u\frac{\partial \epsilon}{\partial x} + w\frac{\partial \epsilon}{\partial z} = \frac{\partial}{\partial z}\left(D_\epsilon \frac{\partial \epsilon}{\partial z}\right) + c_{1\epsilon}\frac{\epsilon}{k}(P_k + (1 - c_{3\epsilon})B_k) - c_{2\epsilon}\frac{\epsilon^2}{k}. \tag{B2}$$

These equations are coupled by the explicit interaction terms in the equations and by the eddy diffusivity $\nu_{3D} = c_\mu k^2/\epsilon$ that feeds back into diffusion coefficients D_k and D_ϵ, as

$$D_k = \frac{\nu_{mol}}{\sigma_{mol}} + \frac{\nu_{3D}}{\sigma_k} \quad \text{and } D_\epsilon = \frac{\nu_{3D}}{\sigma_\epsilon}, \tag{B3}$$

using the turbulence Prandtl-Schmidt numbers $\sigma_k = 1.00$ and $\sigma_\epsilon = 1.30$. The production P_k of TKE is prescribed by gradients in horizontal velocity over the water column (internal shear), with

$$P_k = \frac{\nu_{3D}}{H^2}\left(\frac{\partial u}{\partial z}\right)^2. \tag{B4}$$

The buoyancy flux models the influence of stratification on turbulence by

$$B_k = \frac{g}{H\rho}\frac{\nu_{3D}}{\sigma_\rho}\frac{\partial \rho}{\partial z}. \tag{B5}$$

The relative influence of the production and energy dissipation is implemented using the constants $c_{1\epsilon} = 1.44$ and $c_{2\epsilon} = 1.92$. The buoyancy constant $c_{3\epsilon}$ is a Boolean variable and equals zero in the case of unstable stratification, implemented by

$$c_{3\epsilon} = \mathcal{H}\left(-\frac{\partial \rho}{\partial \sigma}\right), \tag{B6}$$

with Heaviside step-function $\mathcal{H}$, effectively equivalent to a critical Richardson number $\mathrm{Ri}_c = 0$. For estuarine systems where vertical stratification is present, we generally have $B_k \leq 0$, meaning that vertical salinity gradients lead to a reduction in the increase of k. Stable stratification leads to damping of turbulent mixing, whereas unstable stratification leads to higher mixing. The default boundary conditions of Delft3D-FLOW are used, see Deltares (2024).

B2. Eddy Viscosity and Diffusivity in Delft3D-FLOW

In the momentum equation and salinity transport equation, the anisotropic turbulent eddy viscosities and diffusivities are given by

$$A_\mathrm{v} = \nu_\mathrm{mol} + \max\left(\nu_{3D}, \nu_\mathrm{v}^\mathrm{back}\right), \tag{B7}$$

$$A_\mathrm{h} = \nu_\mathrm{mol} + \max\left(\nu_{3D}, \nu_\mathrm{v}^\mathrm{back}\right) + \nu_\mathrm{h}^\mathrm{back}, \tag{B8}$$

$$K_\mathrm{v} = \frac{\nu_\mathrm{mol}}{\sigma_\mathrm{mol}} + \max\left(\frac{\nu_{3D}}{\sigma_\rho}, D_\mathrm{v}^\mathrm{back}\right), \tag{B9}$$

$$K_\mathrm{h} = \frac{\nu_\mathrm{mol}}{\sigma_\mathrm{mol}} + \max\left(\frac{\nu_{3D}}{\sigma_\rho}, D_\mathrm{v}^\mathrm{back}\right) + D_\mathrm{h}^\mathrm{back}. \tag{B10}$$

Here, the subscript notation $_\mathrm{mol}$ denotes molecular effects, superscript notation $^\mathrm{back}$ denotes user-specified constant background values. We use salinity Prandtl-Schmidt number $\sigma_\rho = 0.7$ and molecular Prandtl-Schmidt number $\sigma_\mathrm{mol} = 700$. The background values are given by

$$\nu_\mathrm{v}^\mathrm{back} = 10^{-3}\ \mathrm{m^2/s}, \tag{B11}$$

$$\nu_\mathrm{h}^\mathrm{back} = 10\ \mathrm{m^2/s}, \tag{B12}$$

$$D_\mathrm{v}^\mathrm{back} = 10^{-3}/\sigma_\rho\ \mathrm{m^2/s}, \tag{B13}$$

$$D_\mathrm{h}^\mathrm{back} = 10/\sigma_\rho\ \mathrm{m^2/s}. \tag{B14}$$

The horizontal size of grid cells is much larger than the vertical size, and the larger horizontal background values model some of the subgrid turbulence effects. In fact, model results do not depend on the exact value used as horizontal salinity gradients are small. In turn, horizontal diffusion is small, regardless of the user-specified background values. The nonzero vertical background values dampen short oscillations introduced by boundary conditions and ensure coupling and interaction between layers of different salinity, which would otherwise decouple (Deltares, 2024).

Appendix C: Additional Model Information

C1. Vertical Discretization

Vertical boundary-fitted σ-coordinates are used, for which a layer thickness f_k is defined, resulting in cell height $f_k H$. We use $K = 40$ layers, defined from bottom layer $k = 1$ to top layer $k = K$, and the bottom layer has thickness $f_1 = 0.001$. We choose to linearly increase with Δf per layer in the bottom $\frac{1}{2}K$ layers, and the top $\frac{1}{2}K$ layers have a uniform fraction. This is defined relative to the bottom layer. For general (even) K and bottom layer thickness f_1, this is given by

$$f_k = \begin{cases} f_1 + (k-1)\Delta f, & \text{for } k = 1, \ldots, \frac{1}{2}K, \\ f_1 + \frac{K}{2}\Delta f, & \text{for } k = \frac{1}{2}K + 1, \ldots, K, \end{cases} \tag{C1}$$

for layer thickness increase

$$\Delta f = \left(\frac{3K^2}{8} - \frac{K}{4}\right)^{-1} (1 - K f_1). \tag{C2}$$

C2. Notes on Convergence Study

A convergence study has been carried out in both horizontal and vertical dimensions separately with dunes of $\lambda_d = 125$ m in length and $H_d = 2$ m in height. The vertical resolution is doubled from 10 up to 80 layers while keeping the near-bed cell height fixed in height. Increasing the vertical resolution from 40 to 80 layers changes the total kinetic and potential energy by only 0.1%. For comparison, 40 layers improve the accuracy of the total kinetic energy by around 5% compared to 20 layers.

The horizontal convergence study is performed by halving the horizontal grid size from 80 m down to 1.25 m. A horizontal grid cell width of 5 m increases the accuracy of the flow by only 0.3% compared to a cell width of 10 m. Further grid refinements improve the accuracy to an even smaller degree but drastically increase computational time. More importantly, the salt intrusion length only changes in the order of tens of meters (0.1% of overall salt intrusion length) for grids smaller than the final discretization that uses 10 m.

To verify whether this discretization is also suitable for shorter dunes, the comparison of model performance between 10 and 5 m cell width is rerun for shorter dunes of $\lambda_d = 50$ m. Again, negligible model improvement is observed. The model with the finest horizontal resolution satisfies the hydrostatic consistency condition. Although hydrostatically inconsistent, the coarser model generates equivalent results. Therefore, we conclude that the developed discretization is suitable to model flow and salt transport over estuarine sand dunes.

Appendix D: Mathematical Notation of Operators

Depth averaging: The definition of the depth-averaged value of a variable $\psi(x, z, t)$ is

$$\overline{\psi}(x,t) = \frac{1}{H(x,t)} \int_{z_b(x)}^{\eta(x,t)} \psi(x,z,t)\, dz. \tag{D1}$$

Tidal averaging: We define the tidally averaged (or subtidal) value of a variable $\psi(x, t)$ as the mean over the last tidal cycle with period $T = 2\pi/\omega$ at the end of the simulation (time $t = \tau$), by

$$\langle \psi \rangle(x) = \frac{1}{T} \int_{\tau - T}^{\tau} \psi(x,t)\, dt. \tag{D2}$$

Range over tide: The range over the last tidal cycle of a variable $\psi(x, t)$ is defined by the difference in minimum and maximum for a certain location by

$$(\Delta_t\psi)(x) = \max_t\psi(x,t) - \min_t\psi(x,t). \tag{D3}$$

Estuarine mean: The estuarine mean of a variable $\psi(x,t)$ is defined as the longitudinal mean over the entire estuary by

$$[\psi](t) = \frac{1}{L}\int_0^L \psi(x,t)dx. \tag{D4}$$

Region of salt intrusion mean: The mean of a variable $\psi(x)$ over the ROSI is defined as

$$[\psi]_{\text{ROSI}} = \frac{1}{\max_t(L_s)}\int_0^{\max_t(L_s)} \psi(x)dx. \tag{D5}$$

Note that the above operators are not all commutative.

Appendix E: Normalization Coefficients

To normalize turbulent characteristics, we use the vertical boundary conditions which rely on the shear velocity u_*. In turn, this quantity is linearly related to the velocity u_b near the bed, which we assume to be proportional to the characteristic flow velocity U. Hence, we get the following proportionality at the bed:

$$\tau_b = \rho_0 u_* |u_*| \propto \rho_0 U^2 \tag{E1}$$

$$k = \frac{u_*^2}{\sqrt{c_\mu}} \propto U^2 \tag{E2}$$

$$\epsilon = \frac{u_*^3}{\kappa z_0} \propto \frac{U^3}{z_0}, \quad \Rightarrow \quad K_v \propto \frac{c_\mu}{\sigma_\rho}\frac{k^2}{\epsilon} \propto \left(\frac{\kappa}{\sigma_\rho}\right) z_0 U \tag{E3}$$

Here, κ denotes the Von Kármán constant. These proportionalities to the characteristic velocity U are used to nondimensionalize the first three rows of Figure 6. Stratification is normalized by the seaward salinity s_{sea}. Lastly, inspired by Equation 15, mixing is normalized by $M = s_{sea}^2 hL\omega$.

Data Availability Statement

In this research, version 4.04.01 of the Delft3D-FLOW module is used. The source code of the open-source modelling software is distributed and available via Deltares at https://oss.deltares.nl/web/delft3d. Model input files are made available online (Geerts, 2024).

Acknowledgments
This work is part of the Perspectief Program SALTISolutions, which is financed by NWO Domain Applied and Engineering Sciences in collaboration with private and public partners. We thank Rutger Siemes for helpful discussions on implementation in Delft3D. We thank Yoeri Dijkstra and a second anonymous reviewer for their constructive comments.

References

Berné, S., Castaing, P., Le Drezen, E., & Lericolais, G. (1993). Morphology, internal structure, and reversal of asymmetry of large subtidal dunes in the entrance to Gironde Estuary (France). *Journal of Sedimentary Research*, *63*(5), 780–793. https://doi.org/10.1306/D4267C03-2B26-11D7-8648000102C1865D

Best, J. L., Kostaschuk, R. A., & Villard, P. V. (2001). Quantitative visualization of flow fields associated with alluvial sand dunes: Results from the laboratory and field using ultrasonic and acoustic doppler anemometry. *Journal of Visualization*, *4*(4), 373–381. https://doi.org/10.1007/BF03183900

Biemond, B., de Swart, H., & Dijkstra, H. (2023). Mechanisms of salt overspill at estuarine network junctions explained with an idealized model. *Journal of Geophysical Research: Oceans*, *128*(3). https://doi.org/10.1029/2023JC019630

Biemond, B., de Swart, H. E., Dijkstra, H. A., & Díez-Minguito, M. (2022). Estuarine salinity response to freshwater pulses. *Journal of Geophysical Research: Oceans*, *127*(11), e2022JC018669. https://doi.org/10.1029/2022JC018669

Bijvelds, M. D. J. P. (2001). *Numerical modelling of estuarine flow over steep topography*. Doctoral dissertation, TU Delft, Delft University of Technology. Ipskamp. Retrieved from http://resolver.tudelft.nl/uuid:39c0c858-579a-47fa-a911-4a4114949a11

Bo, T., & Ralston, D. K. (2020). Flow separation and increased drag coefficient in estuarine channels with curvature. *Journal of Geophysical Research: Oceans*, *125*(10), e2020JC016267. https://doi.org/10.1029/2020JC016267

Borsje, B. W., van Wesenbeeck, B. K., Dekker, F., Paalvast, P., Bouma, T. J., van Katwijk, M. M., & de Vries, M. B. (2011). How ecological engineering can serve in coastal protection. *Ecological Engineering*, *37*(2), 113–122. https://doi.org/10.1016/j.ecoleng.2010.11.027

Bradley, R. W., Venditti, J. G., Kostaschuk, R. A., Church, M., Hendershot, M., & Allison, M. A. (2013). Flow and sediment suspension events over low-angle dunes: Fraser Estuary, Canada. *Journal of Geophysical Research: Earth Surface*, *118*(3), 1693–1709. https://doi.org/10.1002/jgrf.20118

Burchard, H., & Rennau, H. (2008). Comparative quantification of physically and numerically induced mixing in ocean models. *Ocean Modelling*, *20*(3), 293–311. https://doi.org/10.1016/j.ocemod.2007.10.003

Campmans, G. H. P., Roos, P. C., Van der Sleen, N. R., & Hulscher, S. J. M. H. (2021). Modeling tidal sand wave recovery after dredging: Effect of different types of dredging strategies. *Coastal Engineering*, *165*, 103862. https://doi.org/10.1016/j.coastaleng.2021.103862

Cheng, H., Chen, W., Li, J., Jiang, Y., Hu, X., Zhang, X., et al. (2022). Morphodynamic changes in the Yangtze Estuary under the impact of the Three Gorges Dam, estuarine engineering interventions and climate-induced sea level rise. *Earth and Planetary Science Letters*, *580*, 117385. https://doi.org/10.1016/j.epsl.2022.117385

Ciofalo, M. (2022). Transient turbulence. In *Thermofluid dynamics of turbulent flows: Fundamentals and modelling* (pp. 109–133). Springer International Publishing. https://doi.org/10.1007/978-3-030-81078-8_7

Cox, J. R., Huismans, Y., Knaake, S. M., Leuven, J. R. F. W., Vellinga, N. E., van der Vegt, M., et al. (2021). Anthropogenic effects on the contemporary sediment budget of the lower Rhine-Meuse Delta channel network. *Earth's Future*, *9*(7), e2020EF001869. https://doi.org/10.1029/2020EF001869

Damveld, J. H., Borsje, B. W., Roos, P. C., & Hulscher, S. J. M. H. (2020). Biogeomorphology in the marine landscape: Modelling the feedbacks between patches of the polychaete worm Lanice conchilega and tidal sand waves. *Earth Surface Processes and Landforms*, *45*(11), 2572–2587. https://doi.org/10.1002/esp.4914

Damveld, J. H., Roos, P. C., Borsje, B. W., & Hulscher, S. J. M. H. (2019). Modelling the two-way coupling of tidal sand waves and benthic organisms: A linear stability approach. *Environmental Fluid Mechanics*, *19*(5), 1073–1103. https://doi.org/10.1007/s10652-019-09673-1

Deltares. (2024). Delft3d-FLOW user manual [Computer software manual]. Retrieved from https://content.oss.deltares.nl/delft3d4/Delft3D-FLOW_User_Manual.pdf

de Nijs, M. A. J., Pietrzak, J. D., & Winterwerp, J. C. (2011). Advection of the salt wedge and evolution of the internal flow structure in the Rotterdam Waterway. *Journal of Physical Oceanography*, *41*(1), 3–27. https://doi.org/10.1175/2010JPO4228.1

de Vriend, H. J., van Koningsveld, M., Aarninkhof, S. G., de Vries, M. B., & Baptist, M. J. (2015). Sustainable hydraulic engineering through building with nature. *Journal of Hydro-environment research*, *9*(2), 159–171. https://doi.org/10.1016/j.jher.2014.06.004

Dijkstra, Y. M., Schuttelaars, H. M., & Burchard, H. (2017). Generation of exchange flows in estuaries by tidal and gravitational eddy viscosity-shear covariance (ESCO). *Journal of Geophysical Research: Oceans*, *122*(5), 4217–4237. https://doi.org/10.1002/2016JC012379

Dijkstra, Y. M., Schuttelaars, H. M., & Kranenburg, W. M. (2022). Salt transport regimes caused by tidal and subtidal processes in narrow estuaries. *Journal of Geophysical Research: Oceans*, *127*(12), e2021JC018391. https://doi.org/10.1029/2021JC018391

Geerts, S. J. (2024). Delft3d-FLOW input files for publication: "Sand dunes as a nature-based solution to mitigate salt intrusion in stratified estuaries". [dataset]. https://doi.org/10.5281/zenodo.10804109

Geurts, B. J. (2022). *Direct and large-eddy simulation*. Walter de Gruyter GmbH and Co KG. https://doi.org/10.1515/9783110532364

Geyer, W. R. (1993). The importance of suppression of turbulence by stratification on the estuarine turbidity maximum. *Estuaries*, *16*(1), 113–125. https://doi.org/10.2307/1352769

Geyer, W. R., & MacCready, P. (2014). The estuarine circulation. *Annual Review of Fluid Mechanics*, *46*(1), 175–197. https://doi.org/10.1146/annurev-fluid-010313-141302

Haney, R. L. (1991). On the pressure gradient force over steep topography in sigma coordinate ocean models. *Journal of Physical Oceanography*, *21*(4), 610–619. https://doi.org/10.1175/1520-0485(1991)021⟨0610:OTPGFO⟩2.0.CO;2

Hansen, D. V., & Rattray, M. M., Jr. (1966). New dimensions in estuary classification. *Limnology & Oceanography*, *11*(3), 319–326. https://doi.org/10.4319/lo.1966.11.3.0319

Hendrickx, G. G., Kranenburg, W. M., Antolínez, J. A. A., Huismans, Y., Aarninkhof, S. G. J., & Herman, P. M. J. (2023). Sensitivity of salt intrusion to estuary-scale changes: A systematic modelling study towards nature-based mitigation measures. *Estuarine, Coastal and Shelf Science*, *295*, 108564. https://doi.org/10.1016/j.ecss.2023.108564

Hulscher, S. J. M. H., & Dohmen-Janssen, C. M. (2005). Introduction to special section on marine sand wave and river dune dynamics. *Journal of Geophysical Research*, *110*(F4). https://doi.org/10.1029/2005JF000404

Jongbloed, H., Schuttelaars, H. M., Dijkstra, Y. M., Donkers, P. B., & Hoitink, A. J. F. (2022). Influence of wind on subtidal salt intrusion and stratification in well-mixed and partially stratified estuaries. *Journal of Physical Oceanography*, *52*(12), 3139–3158. https://doi.org/10.1175/JPO-D-21-0291.1

Kammoun, R., & Abdennadher, C. (2022). Seaport efficiency and competitiveness in European seaports. *Transport Policy*, *121*, 113–124. https://doi.org/10.1016/j.tranpol.2022.04.003

Khojasteh, D., Felder, S., Heimhuber, V., & Glamore, W. (2023). A global assessment of estuarine tidal response to sea level rise. *Science of the Total Environment*, *894*, 165011. https://doi.org/10.1016/j.scitotenv.2023.165011

Klingbeil, K., Deleersnijder, E., Fringer, O., & Umlauf, L. (2022). Basic equations of marine flows. In H. M. Schuttelaars, A. W. Heemink, & E. Deleersnijder (Eds.), *The mathematics of marine modelling: Water, solute and particle dynamics in estuaries and shallow seas* (pp. 1–9). Springer International Publishing. https://doi.org/10.1007/978-3-031-09559-7_1

Knaapen, M. A. F. (2005). Sandwave migration predictor based on shape information. *Journal of Geophysical Research*, *110*(F4). https://doi.org/10.1029/2004JF000195

Kostaschuk, R. A., Best, J. L., & Villard, P. V. (2010). The influence of dunes on mixing in a migrating salt-wedge: Fraser River estuary, Canada. *Earth Surface Processes and Landforms*, *35*(4), 460–465. https://doi.org/10.1002/esp.1928

Kranenburg, W., Van der Kaaij, T., Tiessen, M., Friocourt, Y., & Blaas, M. (2022). Salt intrusion in the Rhine Meuse Delta: Estuarine circulation, tidal dispersion or surge effect? In *Proceedings of the 39th IAHR world congress. June* (pp. 5601–5608). Granada. https://doi.org/10.3850/IAHR-39WC2521711920221058

Lefebvre, A., Ernstsen, V. B., & Winter, C. (2011). Influence of compound bedforms on hydraulic roughness in a tidal environment. *Ocean Dynamics*, *61*(12), 2201–2210. https://doi.org/10.1007/s10236-011-0476-6

Lefebvre, A., Herrling, G., Becker, M., Zorndt, A., Krämer, K., & Winter, C. (2022). Morphology of estuarine bedforms, Weser Estuary, Germany. *Earth Surface Processes and Landforms*, *47*(1), 242–256. https://doi.org/10.1002/esp.5243

Lefebvre, A., Paarlberg, A. J., Ernstsen, V. B., & Winter, C. (2014). Flow separation and roughness lengths over large bedforms in a tidal environment: A numerical investigation. *Continental Shelf Research*, *91*, 57–69. https://doi.org/10.1016/j.csr.2014.09.001

Lefebvre, A., & Winter, C. (2016). Predicting bed form roughness: The influence of lee side angle. *Geo-Marine Letters*, *36*(2), 121–133. https://doi.org/10.1007/s00367-016-0436-8

Lesser, G. R., Roelvink, J. A., van Kester, J. A. T. M., & Stelling, G. S. (2004). Development and validation of a three-dimensional morphological model. *Coastal Engineering*, *51*(8), 883–915. (Coastal Morphodynamic Modeling). https://doi.org/10.1016/j.coastaleng.2004.07.014

Lokin, L. R., Warmink, J. J., Bomers, A., & Hulscher, S. J. M. H. (2022). River dune dynamics during low flows. *Geophysical Research Letters*, *49*(8), e2021GL097127. https://doi.org/10.1029/2021GL097127

Lotze, H. K. (2010). Historical reconstruction of human-induced changes in US estuaries. *Oceanography and Marine Biology an Annual Review*, *48*, 267–338. https://doi.org/10.1201/EBK1439821169-5

MacCready, P., & Geyer, W. R. (2010). Advances in estuarine physics. *Annual Review of Marine Science*, *2*(1), 35–58. https://doi.org/10.1146/annurev-marine-120308-081015

MacCready, P., Geyer, W. R., & Burchard, H. (2018). Estuarine exchange flow is related to mixing through the salinity variance budget. *Journal of Physical Oceanography*, *48*(6), 1375–1384. https://doi.org/10.1175/JPO-D-17-0266.1

MacDonald, D. G., & Horner-Devine, A. R. (2008). Temporal and spatial variability of vertical salt flux in a highly stratified estuary. *Journal of Geophysical Research*, *113*(C9). https://doi.org/10.1029/2007JC004620

Mekonnen, M. M., & Hoekstra, A. Y. (2016). Four billion people facing severe water scarcity. *Science Advances*, *2*(2), e1500323. https://doi.org/10.1126/sciadv.1500323

Németh, A. A., Hulscher, S. J. M. H., & de Vriend, H. J. (2002). Modelling sand wave migration in shallow shelf seas. *Continental Shelf Research*, *22*(18), 2795–2806. https://doi.org/10.1016/S0278-4343(02)00127-9

Pietrzak, J. D., Kranenburg, C., & Abraham, G. (1990). Resonant internal waves in fluid flow. *Nature*, *344*(6269), 844–847. https://doi.org/10.1038/344844a0

Pietrzak, J. D., Kranenburg, C., Abraham, G., Kranenborg, B., & van der Wekken, A. (1991). Internal wave activity in Rotterdam Waterway. *Journal of Hydraulic Engineering*, *117*(6), 738–757. https://doi.org/10.1061/(ASCE)0733-9429(1991)117:6(738)

Pietrzak, J. D., & Labeur, R. J. (2004). Trapped internal waves over undular topography in a partially mixed estuary. *Ocean Dynamics*, *54*(3–4), 315–323. https://doi.org/10.1007/s10236-003-0081-4

Portos-Amill, L., Roos, P. C., Damveld, J. H., & Hulscher, S. J. M. H. (2024). Modeling form roughness induced by tidal sand waves. *Journal of Geophysical Research: Earth Surface*, *129*(5), e2023JF007610. https://doi.org/10.1029/2023JF007610

Ralston, D. K., & Geyer, W. R. (2019). Response to channel deepening of the salinity intrusion, estuarine circulation, and stratification in an urbanized estuary. *Journal of Geophysical Research: Oceans*, *124*(7), 4784–4802. https://doi.org/10.1029/2019JC015006

Stelling, G. S., & van Kester, J. A. T. M. (1994). On the approximation of horizontal gradients in sigma co-ordinates for bathymetry with steep bottom slopes. *International Journal for Numerical Methods in Fluids*, *18*(10), 915–935. https://doi.org/10.1002/fld.1650181003

UNESCO. (1981). Background papers and supporting data on the international equation of state 1980 (Tech. Rep. No. 38). In *Joint panel on oceanographic tables and standards*.

Valle-Levinson, A. (2010). *Contemporary issues in estuarine physics*. Cambridge University Press. https://doi.org/10.1017/CBO9780511676567

van der Sande, W. M., Roos, P. C., Gerkema, T., & Hulscher, S. J. M. H. (2021). Gravitational circulation as driver of upstream migration of estuarine sand dunes. *Geophysical Research Letters*, *48*(14). https://doi.org/10.1029/2021GL093337

van der Sande, W. M., Roos, P. C., Gerkema, T., & Hulscher, S. J. M. H. (2023). Shorter estuarine dunes and upstream migration due to intratidal variations in stratification. *Estuarine, Coastal and Shelf Science*, *281*, 108216. https://doi.org/10.1016/j.ecss.2023.108216

Veerapaga, N., Azhikodan, G., Shintani, T., & Yokoyama, K. (2019). Numerical study on effect of topography, shape, and multi-branch on saltwater intrusion in a conceptual estuary. *Journal of Japan Society of Civil Engineers, Ser. B2 (Coastal Engineering)*, *75*(2), I_19–I_24. https://doi.org/10.2208/kaigan.75.I_19

Veldkamp, T. I. E., Wada, Y., de Moel, H., Kummu, M., Eisner, S., Aerts, J. C. J. H., & Ward, P. J. (2015). Changing mechanism of global water scarcity events: Impacts of socioeconomic changes and inter-annual hydro-climatic variability. *Global Environmental Change*, *32*, 18–29. https://doi.org/10.1016/j.gloenvcha.2015.02.011

Wada, Y., van Beek, L. P. H., Viviroli, D., Dürr, H. H., Weingartner, R., & Bierkens, M. F. P. (2011). Global monthly water stress: 2. Water demand and severity of water stress. *Water Resources Research*, *47*(7). https://doi.org/10.1029/2010WR009792

Zorndt, A. C., Wurpts, A., & Schlurmann, T. (2011). The influence of hydrodynamic boundary conditions on characteristics, migration, and associated sand transport of sand dunes in a tidal environment: A long-term study of the Elbe Estuary. *Ocean Dynamics*, *61*(10), 1629–1644. https://doi.org/10.1007/S10236-011-0452-1